

Liquid-crystal micro-photonics

Igor Muševič

To cite this article: Igor Muševič (2016) Liquid-crystal micro-photonics, Liquid Crystals Reviews, 4:1, 1-34, DOI: [10.1080/21680396.2016.1157768](https://doi.org/10.1080/21680396.2016.1157768)

To link to this article: <https://doi.org/10.1080/21680396.2016.1157768>



Published online: 21 Mar 2016.



Submit your article to this journal [↗](#)



Article views: 535



View related articles [↗](#)



View Crossmark data [↗](#)



Citing articles: 12 View citing articles [↗](#)

Liquid-crystal micro-photonics

Igor Muševič^{a,b}

^aJ. Stefan Institute, Ljubljana, Slovenia; ^bFaculty of Mathematics and Physics, University of Ljubljana, Ljubljana, Slovenia

ABSTRACT

This review presents the main results that were achieved over the past decade in the new field of liquid-crystal micro-photonics. After a general introduction to some aspects of state-of-the-art micro-photonics technologies, nematic colloids are discussed in terms of their self-assembly and photonic properties. Liquid-crystal lasers, based on spatially periodic, liquid-crystal phases, are reviewed, and microlasers based on liquid-crystal microdroplets are presented and discussed. We show that optical microfibres can be self-grown in water/liquid-crystal dispersions and present their waveguiding and lasing properties. The review concludes with a discussion of the resonant transfer of light across different liquid-crystal micro-objects and presents the ultra-fast optical Kerr and STED effects in bulk nematic liquid crystals.

ARTICLE HISTORY

Received 28 December 2015
Accepted 21 February 2016

KEYWORDS

Photonic circuits; liquid crystals; microlasers; microfibers; optical Kerr effect; STED; colloids

1. Introduction to photonics and photonic crystals

The term “photonics” was coined in the article by Yablonovitch and Gmitter entitled “Photonic band structure: The face-centred-cubic case”, published in *Physical Review Letters* in 1981.[1] They introduced the new term “photonic band-gap material” in clear reference to the band-gap structure of the electron energy levels found in solid crystals. It was earlier realised by Yablonovitch and Sajeev John [2,3] that when considering light propagation in optical 3D periodic structures, similar concepts must be applied to photons as to electrons. Therefore, the concept of the Brillouin zone in reciprocal \vec{k} – space has to be introduced because of the periodicity of the dielectric function $\varepsilon(\vec{r})$ of the material in 3D. From this it is clear that the corresponding energy levels for the photons should have a band-like structure, which is a direct consequence of the structural periodicity of the material, as shown schematically in Figure 1. At the time when this work was published, the concept of the photonic band gap was already known and applied in many technical devices, such as the Fabry-Pérot cavities for lasers and interference filters.

In liquid crystals the concept of a photonic band gap was also very well known from the optics of cholesteric [4] and chiral ferroelectric liquid crystals.[5] In a cholesteric (chiral nematic) liquid crystal, the dielectric tensor $\underline{\varepsilon}(\vec{r})$ is periodic along the direction of the helical axis. When considering the solution of the wave

equation describing the propagation of electromagnetic waves along the helical axis, we find an interval of frequencies without solutions for any wave vector \vec{k} . [4,5] This means that a monochromatic light wave with a frequency ω within this interval cannot propagate along the helical axis of the cholesteric. This has an important consequence for the reflection properties of such a material. If light with a frequency within the forbidden frequency interval incidents from an external isotropic medium onto a cholesteric liquid crystal, it will be totally reflected at the interface because it cannot propagate inside the medium. The cholesteric liquid crystal therefore acts as a photonic mirror, which properly reflects the circularly polarised light with a frequency in the forbidden gap.

The introduction of photonic structures in two and three dimensions [1] immediately generated huge interest from the optics community for one simple reason: since the photonic structures act as perfect and lossless materials, they can be used in properly designed structures to guide and re-direct light. Using photonic structures, it is therefore possible, in principle, to construct photonic waveguides, optical microcavities, microlasers and modulators for optical communications and information management. This invention initiated a completely new direction in optical micro-engineering, the goal of which is to design and manufacture photonic analogues of micro-electronic integrated circuits, in which the flow of electrons will be replaced by a flow of photons and which will be controlled by photons. The ultimate

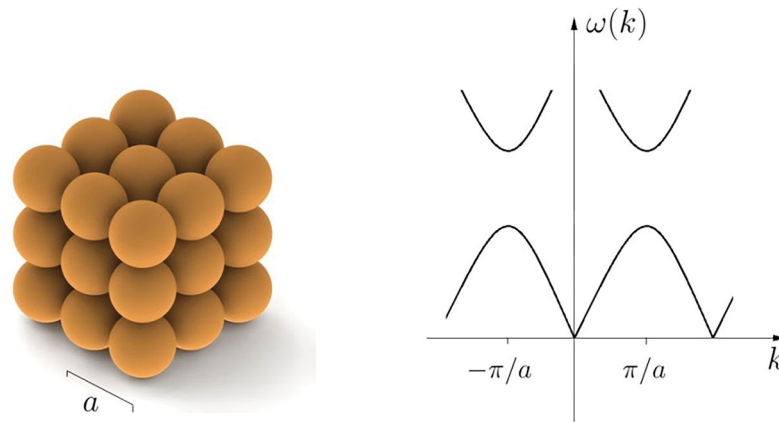


Figure 1. (a) A photonic crystal is a 3D arrangement of dielectric objects with their mutual separation of the order of the wavelength of the light of interest. (b) The dispersion relation for light propagating in such a crystal is periodic in reciprocal space. It exhibits forbidden gaps, where no light with a frequency within this forbidden region can propagate. Image courtesy of E. Zupanič.

aim, therefore, is a future technological platform that will complement, and in many cases replace, microelectronics as we know it today. The importance of such a technological platform is obvious: one of the foundations of our society is the exchange of information, which has expanded over the past 20 years to the point where it has become vital, and is expected to become even more so in our future development. The ever-increasing demands for sharing more information on a worldwide scale have produced serious bottlenecks in information management. The existing infrastructure for managing the flow of information along photonic networks is far from optimal, and costly in terms of energy, thereby limiting the speed of the signal's propagation.

The early stages of research on photonic crystals involved studying colloidal assemblies of photonic crystals in water dispersions with a directed assembly on patterned surfaces,[6] electron-beam microlithography,[7] optoelectronic tweezing of colloids,[8] DNA-assisted colloidal assembly [9] and two-photon polymerisation.[10] Today, we are witnessing the realisation of these ideas in numerous industrial photonic roadmaps, predominantly based on silicon platforms that will merge the photonic large-scale integration technologies with electronic large-scale integration. A new photonic technology is currently being developed on solid-state platforms, which are based on the well-known and highly developed technology of micro-electronic devices, two examples of which [11,12] are shown in Figure 2. Efforts are now being directed towards the development of solid-state integrated photonic devices, which could be used to generate and control the flow of photons on the microscale – and even the nanoscale – by using plasmonic materials. In these devices, photonic crystals are the basic foundation elements; they are used to control and direct the

flow of light, and different methods of fabrication have already been investigated. The first application will most probably be the very fast, on-chip distribution of digital information via photonic highways and photonic floors embedded in standard silicon integrated circuitry in our personal computers.

However, the main drawbacks of solid-state materials for photonic applications are the maturity of the field and its inability to generate a genuine breakthrough for future photonic architectures. The reason for this is that it is difficult, time consuming and expensive to produce truly 3D photonic structures from solid-state materials.[13] Furthermore, the solid state is inherently unable to self-assemble, and it is very challenging to make the surfaces of solid materials smooth enough to reduce the optical losses. The active elements of solid-state photonics are based on electric-charge injection, which results in a high power dissipation, limited frequency response and difficulties in implementing the all-optical control of light by light. In view of the maturity of the field and of the saturation of concepts lacking breakthrough ideas, only incremental advancements of solid-state photonics are likely in the future. There is a clear need for conceptually new ideas and new technological foundations.

While soft matter is an inherently poor electrical conductor and therefore not suitable for electrical applications, it is an excellent optical material, which is surprisingly robust, capable of self-repairing, healing and self-assembling in fascinatingly complex photonic architectures, as is evident in modern liquid-crystal displays, for example. This has led to the idea [14,15] that we could use liquid crystals and soft matter in general, to design and construct photonic integrated devices made entirely of soft matter. With this aim in mind, dispersions of silica microcolloids in nematic liquid crystals were first used

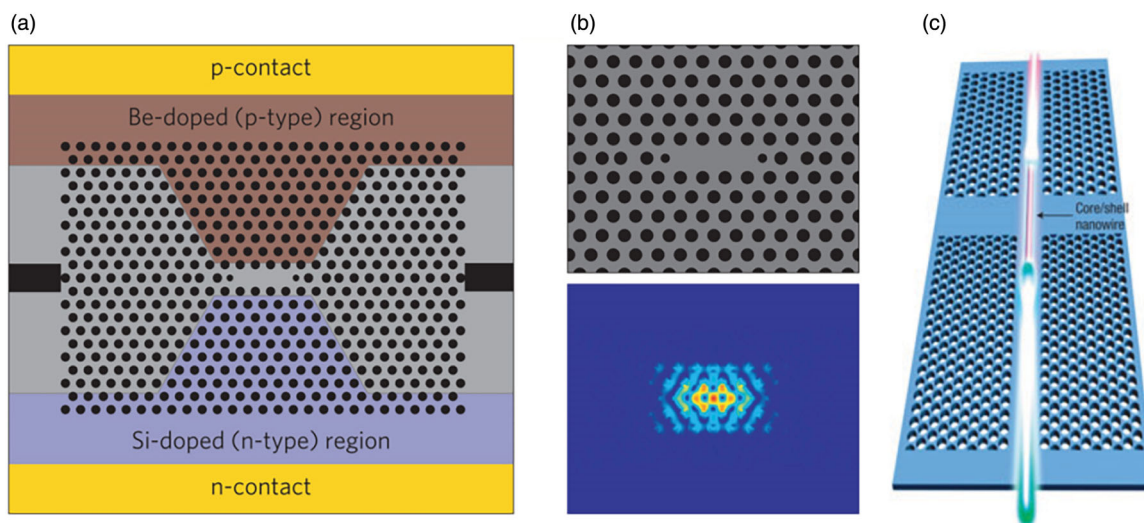


Figure 2. Microphotonic structures based on photonic crystal concepts. (a) Schematic of an electrically pumped photonic-crystal laser. The p-type doping region is indicated in red, and the n-type region in blue. The width of the intrinsic region is narrow in the cavity region to direct the current flow to the active region of the laser. (b) Modified three-hole defect photonic-crystal cavity design (top) and a finite-difference time-domain method simulation of the E-field of the cavity mode in such a structure (bottom). Reprinted by permission of Macmillan Publishers Ltd: Nature Photonics [11] copyright (2011). (c) Schematic of a CdS/CdSe core/shell nanowire facing two different straight-line-defect waveguides. The upper waveguide is designed to guide the red light and to filter out the green light, whereas the lower waveguide is designed to guide the green light and to filter out the red light. Reprinted by permission of Macmillan Publishers Ltd: Nature Photonics, Ref. [12], copyright (2008).

to assemble a variety of colloidal photonic crystals in 1D, 2D and 3D. Later, it was realised that dispersions of liquid crystals in immiscible carrier fluids offer a fascinating variety of self-assembled microdroplets and microfibrils that operate as optical microresonators, microlasers and optical waveguides. Using colloidal assembly, these fluid micro-elements can be further assembled on a larger hierarchical level into all-fluid optical microcircuits.

The purpose of this review is to provide an overview of the ideas, experiments and results, all of which support the conjecture that it is possible to produce real, functioning photonic devices based exclusively on soft matter, including liquid crystals.

2. Photonic structures assembled from nematic colloids

The first evidence for the self-organisation of colloidal particles in a nematic liquid crystal was reported by Cladis, Pieranski and Rault,[16,17] who decorated the free surface of a nematic liquid crystal with small bubbles. They observed the spontaneous organisation of these bubbles into regular chains that were following the overall molecular orientation at the surface of the liquid crystal. A similar example of surface patterning by incorporating glycerol microdroplets is shown in Figure 3, where the small droplets are floating at the free surface of a nematic liquid crystal. This spontaneous chaining of foreign particles in liquid crystals is clear evidence of a new



Figure 3. Decoration of the free surface of a nematic liquid crystal with small glycerol droplets that spontaneously assemble into chains. This chaining is clear evidence for a force between the droplets. These forces are due to the elastic distortion of the nematic liquid crystal, which aligns along the closed surface of each glycerol droplet. Image courtesy of V. S. R. Jampani.

type of force between the colloidal inclusions in liquid crystals.

Whereas the decoration of liquid-crystal surfaces with foreign particles is a practical method for visualising the director field, the first study of the forces between the inclusions of nematic liquid crystals was performed by Poulin et al.[18] They were studying dispersions of water

in nematic liquid crystals and observed the spontaneous chaining and stabilisation of individual water droplets.

It was observed that each pair of droplets was separated by a topological point defect. The presence of this defect is crucial for the stability of the water chains in nematic liquid crystals and prevents their coalescence. The stability of the chains of particles also demonstrates the strength of the force exerted by the nematic liquid crystal on the colloidal particles. This pair-interaction force obviously exceeds the forces due to the thermal motion of the fluid and the pair-binding energy is much stronger than the thermal energy $k_B T$.

The spontaneous chaining of the colloidal particles in nematic liquid crystals remained unexplored for nearly a decade, because there were no techniques for the non-contact manipulation of each colloidal particle in the liquid crystal or for studying their interactions. However, the year 2000 saw the technique of laser tweezers being introduced to liquid crystals as a new and powerful tool for the controlled manipulation of colloidal particles in liquid crystals.[19–24] It was shown that the laser tweezers could trap and move practically any kind of micrometre-sized particle in the nematic liquid crystal using light. Using these laser tweezers, it was possible to study and measure the forces and interactions between a pair of particles and to explore and understand the role of the different topological defects that are responsible for the colloidal interactions in nematic liquid crystals.

The nature of the force between colloidal particles in a nematic liquid crystal has its origin in the orientation of the liquid-crystal molecules at the surface of each particle. Because this is a closed surface and the molecules are forced to align equally at all points on the surface, there is a frustration of the liquid crystal as it tries to fill the space with liquid-crystal molecules. It turns out that this is impossible without creating topological defects in the vicinity of the included particle. These defects appear in the form of points accompanying the colloidal particle or small loops encircling them, and besides topological defects, the colloidal inclusion is surrounded by a large area of elastically distorted liquid crystal. When two colloidal particles are brought together, each of them carrying this elastically distorted liquid crystal, their regions start to overlap. As a result of this overlapping, the total free energy of the colloidal pair depends on their separation. This means that a force is generated between the colloidal particles, which is elastic in origin and is responsible for the self-organisation of nematic colloids. Remember that a generalised force between two particles is a negative derivative of the total free energy of the pair with respect to their separation.

Depending on the type of surface ordering, spherical microparticles in nematic liquid crystals exhibit different

topological defects. For perpendicular surface anchoring, there are two kinds of possible defects, i.e., points and rings, and they are accompanied by different elastic distortions, called the dipolar and quadrupolar elastic distortions. The pair interaction depends on the symmetry of this elastically distorted region and allows for the self-assembly or directed assembly of colloidal particles into linear or kinked chains, or 2D dipolar and quadrupolar colloidal crystals,[25–29] as shown in Figure 4(a)–(d). These colloidal structures resemble the photonic crystalline structures shown in Figure 2(a)–(c).

All these photonic-like colloidal structures were assembled with the use of laser tweezers. Once assembled, they are perfectly stable, since the pair-binding energy exceeds thousands of $k_B T$ energy per micrometre-diameter colloidal particle. In all the above-mentioned cases, the binding forces are generated by topological defects, which are singularities of the order parameter field. These forces are of long range with a power-law decay, generating structural forces that are able to bind even nanometre-sized particles, as demonstrated recently.[30] This means that building a photonic circuits for optical or infrared wavelengths is both realistic and technologically feasible. The required photonic crystal-lattice periodicity is, for this purpose, of the order of 500 nm and typically 100-nm-diameter particles should constitute these photonic structures. The colloidal forces in nematic colloids not only provide the assembly of 2D photonic-like structures, as it was demonstrated recently that 3D nematic colloidal crystals could be assembled as well.[31] An example of the assembly of a 3D nematic colloidal crystal is shown in Figure 5(a). In consecutive images it is clear how the laser tweezers (indicated by a tiny red cross) are used to pull together prefabricated blocks of colloidal crystals, floating in the nematic liquid crystal. Once they are brought close enough (panel 3 of Figure 5(a)), these two blocks spontaneously assemble into a perfectly aligned 3D crystal. The crystal structure is represented in Figure 5(b), revealing the tetragonal symmetry of the unit cell.

Point and loop defects are not the only sources of colloidal pair interaction in nematic liquid crystals. It was as a surprise when the laser tweezers were used to quench a small area of a nematic liquid crystal containing silica particles from the isotropic phase and novel colloidal structures were observed when this quenched region cooled down into the nematic liquid crystal.[32] As already mentioned, topological defects in the form of singular loops surrounding the colloidal particle were known (Saturn ring, Ref. [33,34]), but it was unexpected to find that a single defect loop could extend over several colloidal particles, forming a tightly entangled colloidal pair. Numerical simulations based on the Landau-de

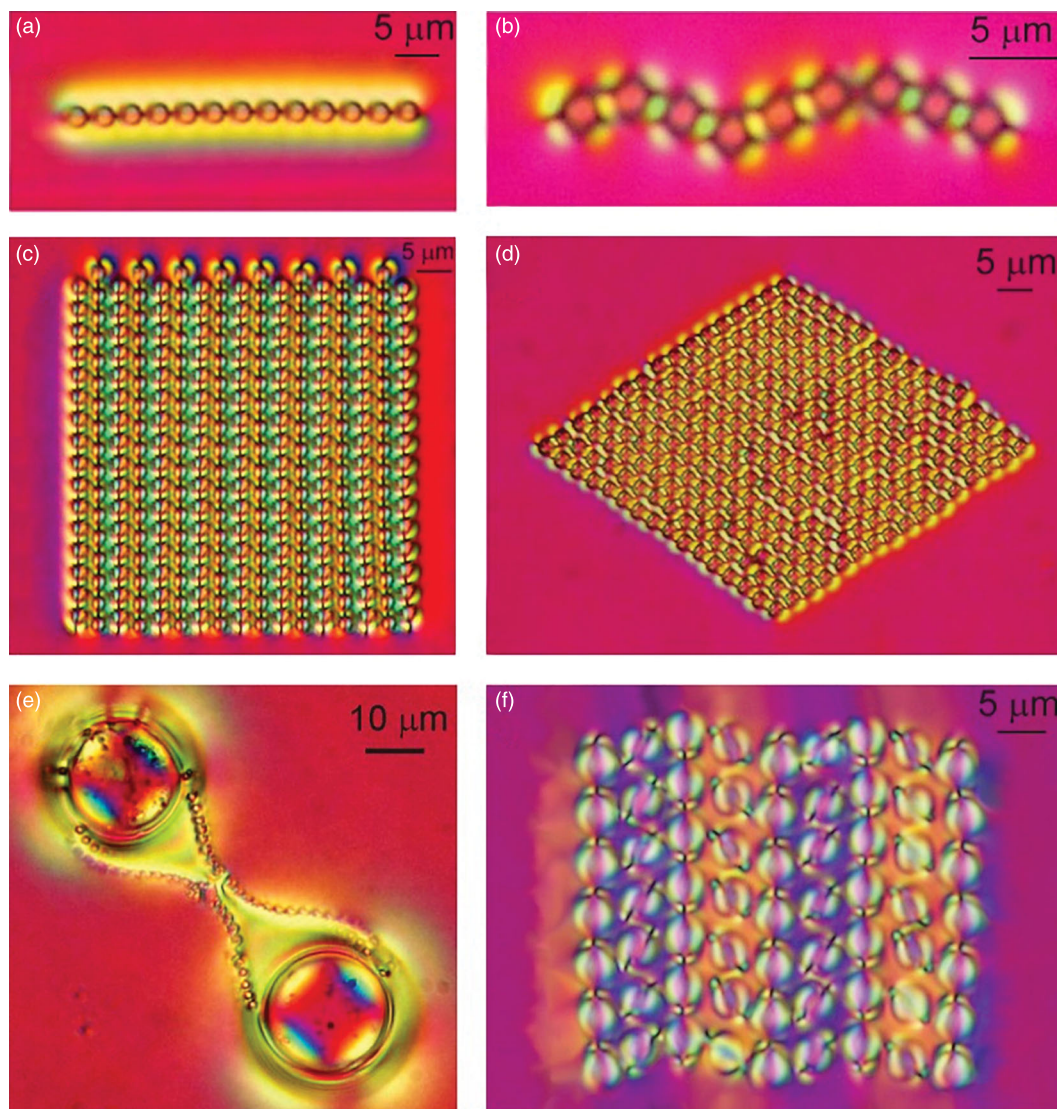


Figure 4. (a) 1D chains of dipolar colloidal particles, and a kinked chain (b), made up of quadrupolar particles. 2D nematic colloidal crystals assembled from dipolar colloidal particles (c), quadrupolar colloidal particles (d) or a mixture of both (f). (e) Hierarchical colloidal structures are formed in a mixture of small and large colloidal particles, where smaller particles are trapped into the defect lines surrounding the larger particles.

Genies theory predicted such entangled states [32,35,36] and three topologically different entangled structures were identified in planar nematic cells filled with non-chiral nematic liquid crystal.

The entanglement of colloidal particles by the topological defect loops is a fundamentally different phenomenon from dipolar or quadrupolar interactions, because sharing the same topological defect loop gives rise to a force between the entangled colloids. The entanglement provides a strong, string-like force between the colloidal particles, and the interaction is nearly an order of magnitude stronger than the dipolar colloidal interaction. Colloidal entanglement is a topologically interesting phenomenon and is particularly rich in chiral

nematic colloids. Tkalec et al. [37] found that chiral nematic liquid-crystal (CNLC) colloids could be entangled to form knots and links, spanned on the scaffold of colloidal particles. Knots and links in chiral nematic colloids are two of very few examples of the realisation of these abstract objects in the real world, and were originally reported in chiral nematic liquid crystals by Bouliand in 1974.[38] Recently, knots and links have also been observed in highly chiral nematic colloids,[39] with the helical pitch comparable to the colloidal diameter. Whereas knotted and linked chiral nematic colloids are primarily interesting because of their rich topology, they might also be interesting for future photonic applications, mixing the topology of matter and the light field.

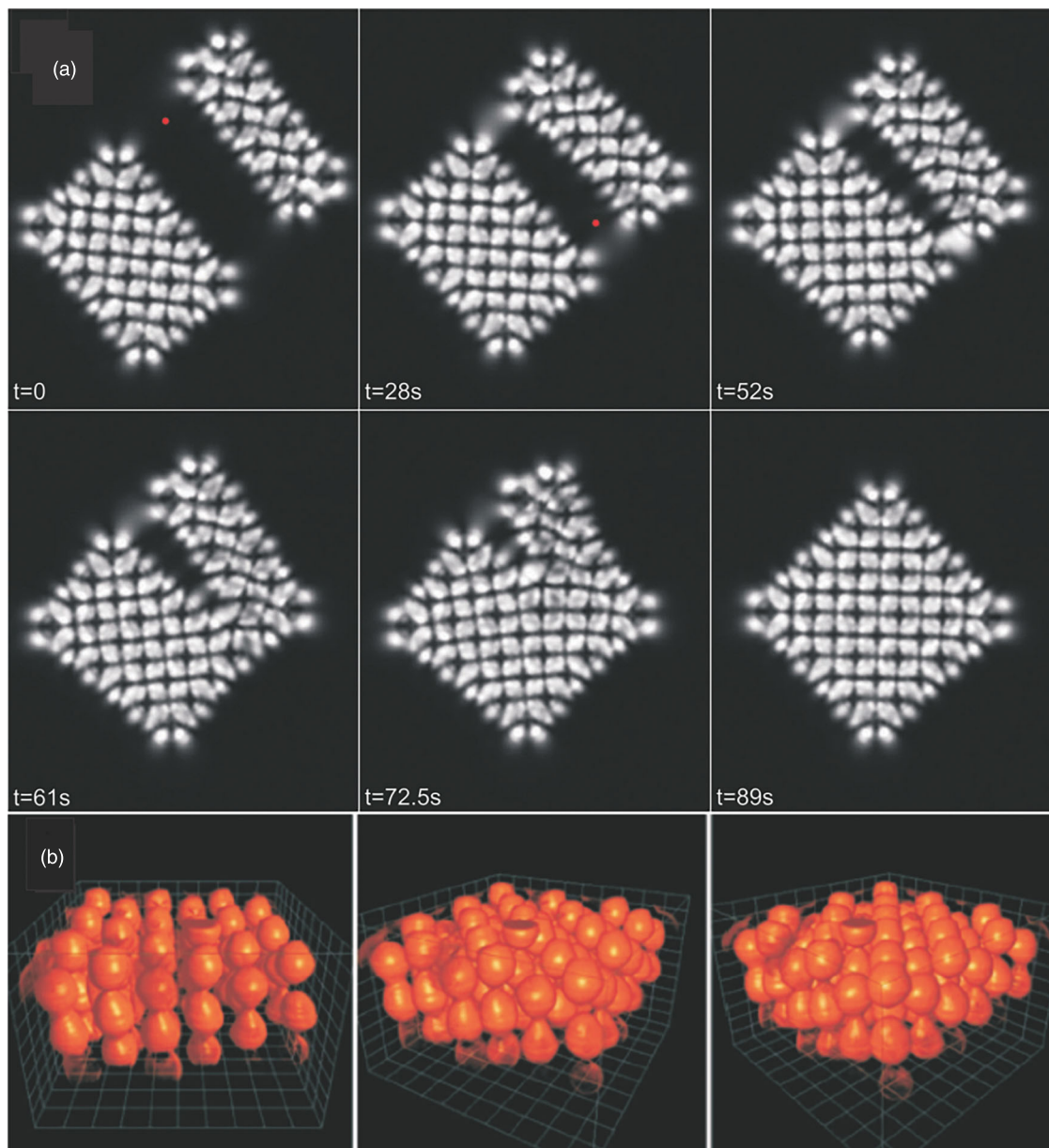


Figure 5. (a) Laser-tweezers assembly of a 3D dipolar colloidal crystal observed under crossed polarisers. Colloidal blocks of $2 \times 6 \times 3$ and $4 \times 6 \times 3$ particles assemble into the final $6 \times 6 \times 3$ dipolar colloidal crystal. The assembly during the initial stage was guided by the laser tweezers until the blocks started to attract themselves. In all the images, the small red dot is the optical trap, used to direct the colloidal assembly. (b) 3D representation of the fluorescence confocal polarised microscopy image of a $6 \times 6 \times 3$ three-dimensional dipolar colloidal crystal, revealing the tetragonal symmetry of the unit cell (image courtesy of A. Nych).

3. Lasers based on the photonic properties of periodic liquid-crystal phases

Many liquid-crystalline phases exhibit vivid colours of reflected light when illuminated by white light. An example is the well-known CNLC phase (cholesteric), where the colour of the reflected light is directly related to the helical organisation of the liquid-crystal molecules in this phase. The optical properties of chiral nematic liquid crystals were thoroughly studied in the past, and we understand that they are due to the spatial periodic

organisation of chiral liquid-crystalline phases. In a spatially periodic liquid-crystal structure, the colour and polarisation of the reflected light are caused by the photonic band structure of the dispersion relation for light propagating along the helical axis of this phase. The CNLC phase forms a 1D photonic structure with a band gap centred on the wavelength that is directly related to the inverse helical pitch of this phase (see Figure 6(a)). This band gap exists only for light that is circularly polarised and has the same sense of rotation as the helical

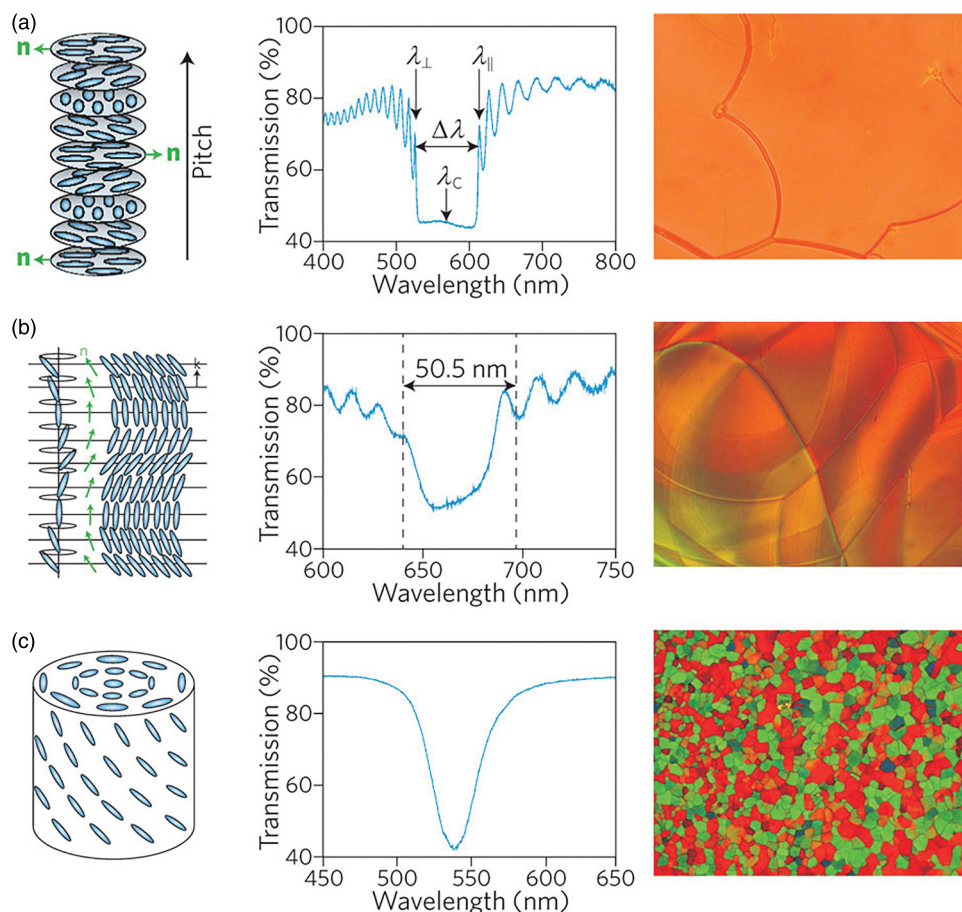


Figure 6. Structure and photonic band-gap properties of different liquid-crystal phases. (a) Chiral nematic. (b) Chiral smectic. (c) Blue phase. The structure of the director field is shown for each phase on the left-side panels. The transmission spectrum for white light of each phase is shown in the middle panels. The micrographs of the texture between the crossed polarisers are shown on the right-side panels. In blue phases the double-twist cylinders form a 3D regular array of defects, which gives rise to Bragg reflections. Reprinted by permission of Macmillan Publishers Ltd: Nature Photonics (reference [40]), copyright (2010).

structure. A similar 1D photonic structure is observed in the chiral smectic C^* liquid-crystal phase, where the band gap appears for the same reason as in the CNLC phase (Figure 6(b)). In both cases, the helical organisation of the phase is directly related to the chirality of the molecules constituting the phase. In both cases, the helical organisation of the molecules causes a spatially varying index of refraction, which gives rise to Bragg reflections for the light propagating along the helix. This structural periodicity, which is a consequence of the molecular chirality, is therefore responsible for the onset of the photonic band gap and the wavelength-dependent reflection coefficient. A similar phenomenon of the photonic band gap is observed for the blue phases I and II, which exhibit a 3D periodic structure. In these phases, an incomplete photonic band gap exists for the light propagation in each of the three dimensions, as shown in Figure 6(c).

A spatially periodic liquid-crystal phase that possesses a photonic band gap is an essential ingredient for lasers based on liquid crystals. In liquid-crystal lasers,

the spatially modulated structure provides an optical resonator, where the resonances are due to the spatial periodicity of the structure. In addition to having an optical resonator, which provides multiple passes of light through the resonator, by Bragg reflection an optical gain material has to be added to the resonator to amplify the light. In such a complex structure, there are two important physical mechanisms taking place when light with a given frequency is travelling along the direction of the spatial modulation. If the frequency of the light is within the forbidden frequency gap of the structure, the light will be Bragg-reflected back and forth within the resonator. However, if dye molecules are added and uniformly distributed within this spatially periodic structure, the light can be amplified by the process of stimulated emission. In order for this process to take place, the dye molecules must first be excited into higher electron energy levels, which involves illuminating the resonator with dye molecules using short light pulses. When these molecules emit fluorescent photons, they are Bragg-reflected by the

surrounding periodic lattice and with a certain probability they create another identical photon through the process of stimulated emission from another excited dye molecule. The process of light amplification by stimulated emission in such distributed-feedback photonic structures will eventually result in lasing. This will take place when the light amplification exceeds the optical losses in the photonic structure, which plays the role of the distributed-feedback optical resonator. There are, therefore, two necessary components to form liquid-crystal lasers: the periodic structure, forming the optical resonator, and the dye molecules, playing the role of the optical amplification medium. Such a laser is usually triggered by an external pulsed-laser source, and the liquid-crystal laser emits the laser light along the direction of the periodic modulation of the refractive index. Figure 7 shows an example of lasing in a cell with a cholesteric liquid crystal and different fluorescent dyes. This cell is locally illuminated with short-wavelength excitation laser pulses (not visible in the images) and a cholesteric structure generates a strong laser beam, which propagates along the direction of the helical axis. The colour of the laser light is defined by the helical period of the structure and the corresponding position of the photonic band gap in the spectrum. Because in Figure 7 the pitch depends on the position of the cell, different laser colours can be generated by exciting different spots on the cell. In all cases, liquid-crystal lasers are dye lasers, and have all the advantages and disadvantages associated with such lasers.

Lasers based on liquid crystals have been well known for a long time [40]; their basic advantage is their spontaneous formation of structures. The first dye-doped cholesteric liquid-crystal lasers were realised

independently by Kopp et al. [41] and later by Taheri et al. [42] Later on, the lasing was realised in a series of liquid-crystal structures and phases, such as the chiral ferroelectric smectic phase,[43,44] liquid-crystal polymers,[45–49] chiral nematic elastomers,[50] cholesteric glasses,[51,52] an intermediate phase between the chiral nematic phase and the smectic A phase [53] 21, and blue phases I and II.[54–56]

Figure 8 shows an example of the blue-phase (BP) II laser. In a BP, double-twist cylinders of the chiral BP material (Figure 8(a)) are packed together into a cubic lattice, forming a 3D-photonic band-gap material, interpenetrated by defects. These band-gap properties are easily recognised by the strong colouring of the BP II single crystals, which is due to a strong Bragg reflection from the periodic photonic structure. Figure 8(c) shows examples of such crystalline platelets, as observed in reflection. The different colours are due to the different planes for the reflection of light from the BP II lattice. If such a crystal is doped with a fluorescent dye, and the dye is then excited with an external pulse laser, the crystal will start lasing about some threshold pumping energy. Figure 8(d) shows the spectra of light collected from such a small crystal platelet, taken at different levels of pump energy. At low levels of pumping energy, the spectra are simply a broadband fluorescence of dye molecules added to this material. There is clearly a threshold where the measured spectrum changes, because a sharp line appears in the spectrum, which increases with increasing pumping energy. This is typical for the onset of lasing from distributed-feedback dye lasers, which can be recognised by the characteristic knee in the measured output intensity, shown in the inset of Figure 8(d).

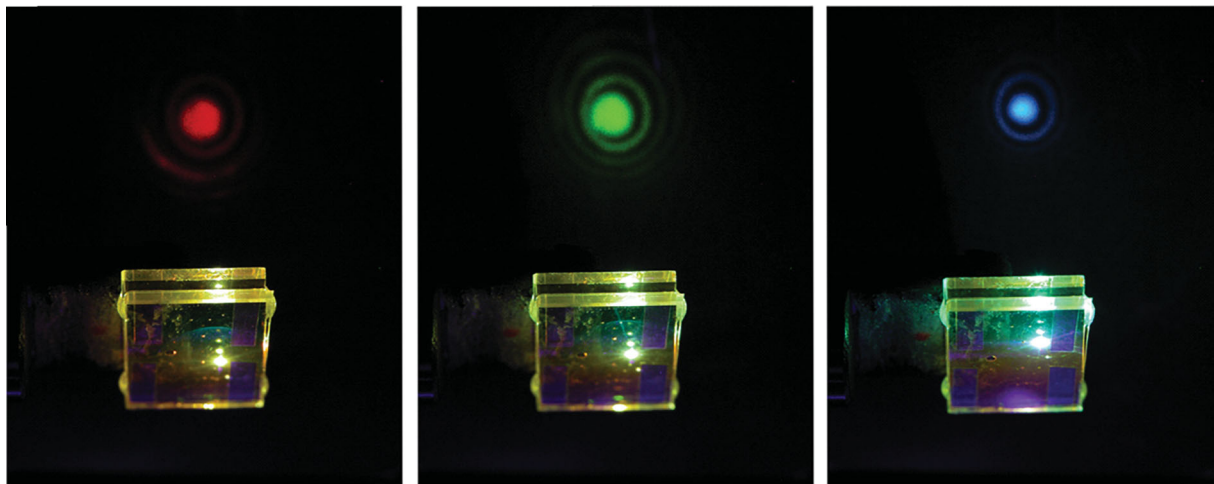


Figure 7. Position-sensitive wavelength of the emitted laser light in a cholesteric liquid-crystal dye laser covering the full visible range. Two different cholesteric liquid crystals with two different dyes were injected into the glass cell from opposite sides. In this way, the pitch gradient was spontaneously achieved across the cell via the mixing of both liquid crystals. By pumping the dye laser at different positions, different wavelengths of the output light were selected. Image courtesy of Hideo Takezoe.

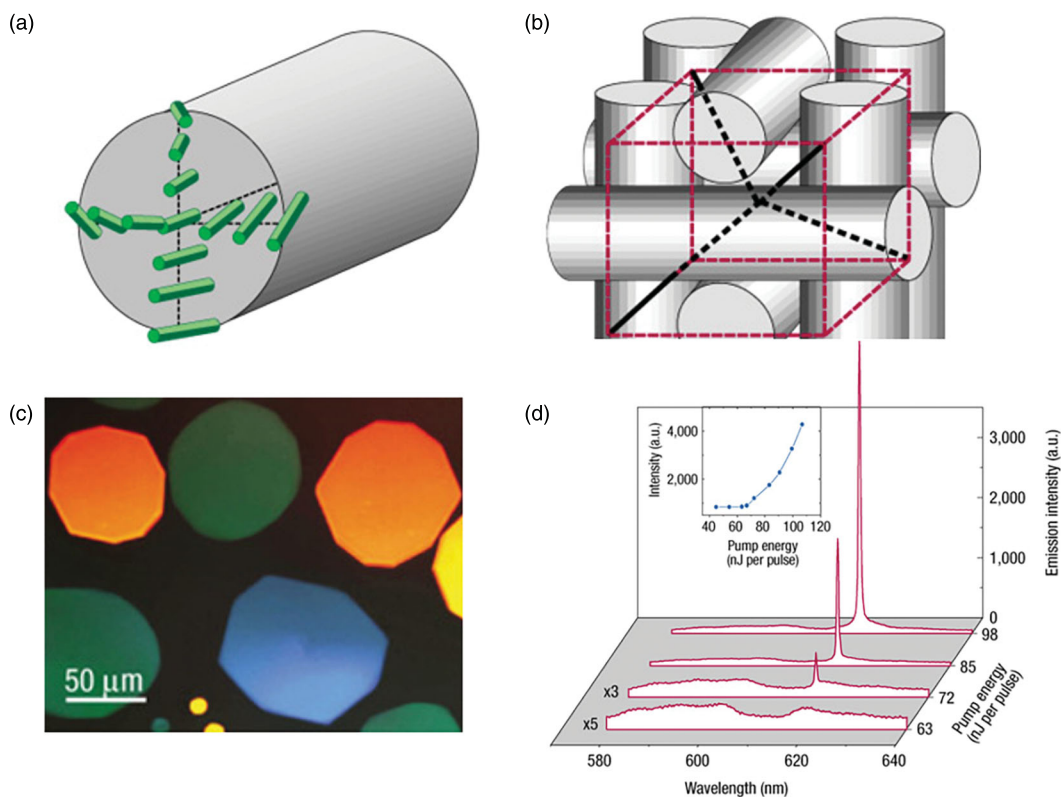


Figure 8. (a) The director field inside a double-twist tube of the BP. (b) Stacking of double-twist tubes and unit cell (red) and disclination lines (black). (c) BPII single crystals at 24.6°C of a mixture consisting of the nematic liquid crystal E48 and the chiral dopant CB15. (d) Fluorescence and lasing spectra at different pump energies. At the threshold for lasing, a sharp spectral line pops out from the fluorescent background. The inset shows the emitted intensity at a wavelength of 617.23 nm versus the pump energy. The characteristic “knee” corresponds to the onset of lasing. Reprinted by permission of Macmillan Publishers Ltd: Nature Materials (reference [40]), copyright (2002).

In all these phases, not only was the lasing demonstrated, but also various methods for tuning the lasing wavelength. The liquid-crystal lasers could be tuned by changing the external temperature,[57–59] the ultraviolet illumination,[60–62] the mechanical stress,[49,51] and the application of an external electric field.[44,63–66] The liquid-crystal dye lasers described in these studies exhibit a very small thickness of the order of 10 micrometres, but have large lateral dimensions, as they are fabricated in centimetre-sized glass cells filled with liquid crystals. The actual active area of such a laser is in fact relatively small, as the lasing takes place only from the region of the liquid crystal, which is illuminated with an external pumping laser. This area is small: of the order of tens of micrometres. One obvious question is how to reduce the dimensions of such lasers to micrometre-sized objects?

A natural way of producing micrometre-sized objects from liquid crystals is to disperse the liquid crystal in another liquid in which it is immiscible. Then, because of the chemical incompatibility, the liquid crystal will spontaneously form micrometre-sized droplets with a perfect spherical shape, as shown in Figure 9. It was

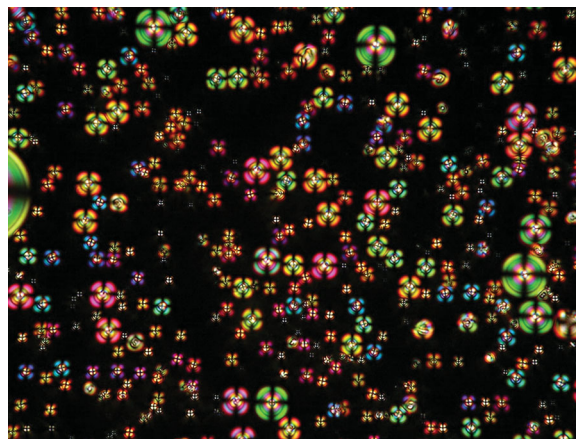


Figure 9. Millions of microdroplets of a nematic liquid crystal in a thin layer of PDMS, as seen under crossed polarisers. Image courtesy of M. Humar.

recently demonstrated that such small droplets of a nematic liquid crystal, or a cholesteric liquid crystal, dispersed in an immiscible fluid could be used as optical microcavities that are tuneable with an electric field [67] and microlasers.[68] If the nematic liquid crystal is

replaced by a chiral nematic liquid crystal with a helical period in the range of optical frequencies, we can obtain an unusually structured droplet that acts as a three-dimensional Bragg-onion microresonator. In this case, the liquid-crystal molecules at the interface are oriented parallel to the interface, and the helical structure is formed all the way to the centre of the droplet, where a topological defect is situated. We should also mention the recent demonstration of self-assembled optical microfibres from smectic-A liquid crystals. In combination with tuneable optical microcavities and microlasers, these findings are the basis for future photonic devices based on soft matter.

4. Optical microresonators made of LC droplets: light is confined to a microcavity

In spherical microresonators [69] the light is trapped inside the microsphere by total internal reflection at the interface between the microsphere and the surrounding medium. We can consider that the light is circulating inside the microsphere with consecutive total internal reflections at the interface. The resonance condition for the circulating light is fulfilled if the light reaches the point of origin with the same phase after one circulation. These kinds of optical resonances are referred to as whispering-gallery modes (WGMs) or morphology-dependent resonances and are observable in resonators with other shapes, not only spherical. In these resonators the optical modes are confined to very small volumes and the resonators may have very high Q-factors of the order up to 10^{10} . These devices are extremely interesting for applications in laser sources, active filters and all-optical switches.[70] Of utmost importance are the tuneable resonators, in which the resonance frequency is tuned by size, shape, and temperature, or preferably by the electric field. The largest frequency shifts can be obtained by the mechanical shift control,[71,72] but this control is slow, inaccurate and not practical for real applications. Solid-state microresonators can be tuned electrically; however, the shift of the resonance frequencies at reasonable electric fields is usually relatively small. Another option is tuning solid-state microresonators by controlled heating and temperature-induced changes, which is energetically very costly,[73] or using the electro-optic effect.[74]

It was recently demonstrated [67] that small nematic droplets embedded in a polymer matrix are low-loss optical microresonators, which can be tuned efficiently by an external electric field. They were prepared by mixing a small amount (several per cent by weight) of a fluorescently labelled nematic liquid crystal, such as E12 or 5CB, and polydimethylsiloxane (PDMS). These kinds

of mixtures are well known from previous studies of polymer-dispersed liquid crystals (PDLCs) and electric-field-controlled scattering in these materials. However, in those studies, the droplets were rather small (less than a micrometre) to induce a strong scattering of light in the off-state, which could be switched into the transparent state by an electric field. Furthermore, in PDLC dispersions, huge numbers of densely packed droplets were used in order to obtain a strong scattering of the light and a milky appearance of the PDLC film. In our case, we are considering the optical properties of a single nematic droplet with molecules oriented perpendicularly at the surface of the droplet, which results in a radial topological defect in the centre of the droplet.

A micrograph of a typical microdroplet of a nematic liquid crystal in polymer is shown in unpolarised light and between crossed polarisers in Figure 10(a) and 10(b), respectively. The droplet was prepared by mixing a small amount of a fluorescently labelled nematic liquid crystal into a PDMS matrix.

Figure 10(b) shows a uniaxial dark cross that occurs when the droplet is observed between the crossed polarisers and which clearly indicates radial organisation of the director field inside the droplet. There is a topological defect, also called a radial “hedgehog” defect,[75] in the centre of the droplet, and the structure is uniformly splayed. When the dye-doped nematic liquid-crystal microdroplet of $10\ \mu\text{m}$ diameter is illuminated with light that is focused on the interior close to the equator, we clearly observe a ring of light in the interior of the droplet, which strongly emits light on the other side of the equator, as shown in Figure 10(d). The observed fluorescent ring and the strong emission of light from that ring clearly demonstrate that this is due to the WGMs. The analysis of the polarisation properties shows that the WGM ring is polarised radially. Both the intensity profile and the polarisation properties indicate that the WGM is therefore a transverse magnetic (TM) mode, which is in agreement with the structure of the nematic liquid crystal inside the droplet.

The polarisation spectrum can be understood from the structure of the dielectric tensor of the liquid crystal at optical frequencies. The dielectric tensor is uniaxial with the principal axis $\varepsilon_{xx} = \varepsilon_{yy}$ and ε_{zz} in the coordinate system presented in Figure 11. The optical axis is along the z -direction and the corresponding refractive indices are $n_o = \sqrt{\varepsilon_{xx}}$ and $n_e = \sqrt{\varepsilon_{zz}}$. The TM modes therefore “see” the extraordinary refractive index, typically $n_e \approx 1.7$, which is much larger in a nematic liquid crystal than the ordinary refractive index, typically $n_o \approx 1.5$. The TE modes see a much lower index contrast with respect to the surroundings,

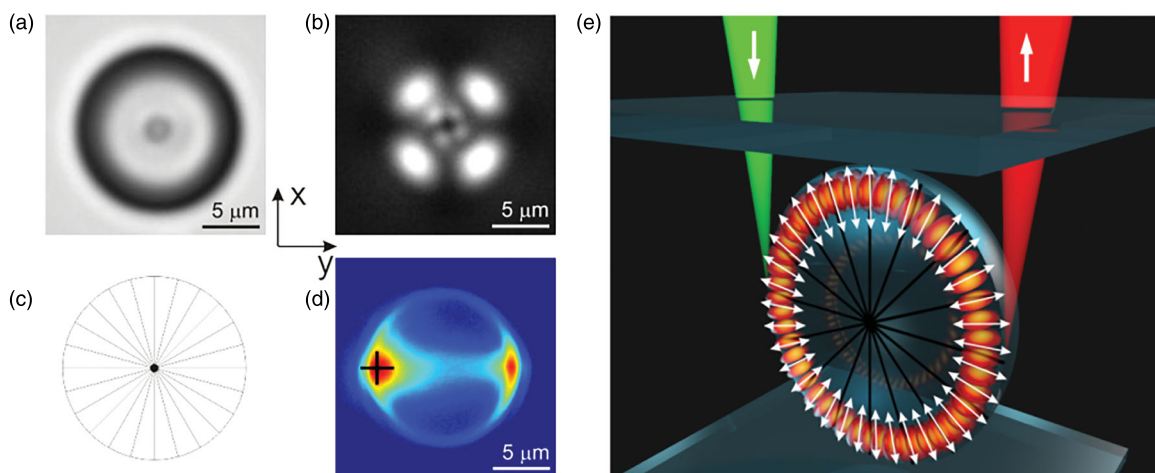


Figure 10. WGM resonances in nematic liquid-crystal microdroplets. (a) Microdroplet of nematic liquid crystal E12 in PDMS. (b) The same droplet under crossed polarisers. (c) Structure of the director field inside the microdroplet with perpendicular surface anchoring. The lines representing the director field merge in the centre, where a radial “hedgehog” defect is located. (d) Light intensity under illumination from a strongly focused beam of the Ar^+ laser tweezers, which is illuminating the left-side rim of the droplet indicated by the black cross. Note the strong intensity on the other side of the rim, indicating the circulation of the light inside the droplet. (e) Schematic view of WGMs in a liquid-crystal droplet with the electric field oscillating in the radial direction. The green beam is the excitation light; the red beam indicates the detected light.

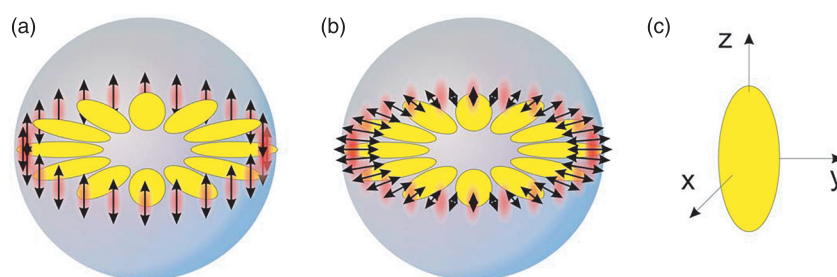


Figure 11. Schematic view of the electric field oscillations in (a) transverse electric (TE) and (b) TM WGMs. The prolate yellow-coloured objects represent the liquid-crystal molecules, pointing with their axis in the radial direction. (c) The reference frame with the representation of the uniaxial dielectric tensor of the nematic liquid crystal with eigenvalues $\epsilon_{xx} = \epsilon_{yy}$ and ϵ_{zz} . Image courtesy of M. Humar.

and are therefore leaky modes with very low intensities. Accordingly, the TM modes are dominant, and their radial polarisation is in agreement with the experimental observations.

The spectrum of light emitted from a 10–12- μm -diameter nematic liquid-crystal microdroplet in PDMS is presented in Figure 12. The WGM resonances are clearly observed above the fluorescent background. For droplets of a smaller size, only the TM modes are supported by the resonator, and this set of modes usually corresponds to the fundamental, lowest frequency of the WGM TM modes with radial number $n = 1$. Here, n is the radial number of the mode, which determines the number of maxima in the radial intensity distribution of the modes inside the sphere. For somewhat larger droplets, shown in Figure 12(b), an additional set of

modes is observed, which correspond to higher radial TM modes. We expect that in extremely large droplets, the TE modes would appear as well, as the mode losses are inversely proportional to the radius of curvature of the resonator.

The linewidth of the WGM resonances in nematic liquid-crystal droplets in PDMS ($n = 1.43$) is typically 0.055 nm, which corresponds to a Q-factor of the cavity of the order of 12,000. The most probable reason for the optical losses is the thermally induced orientational fluctuations of the nematic director. The Q-factor depends on the temperature and size of the droplet, which determine the radiative losses due to the interfacial curvature. For smaller droplets (10 μm), the Q-factor is between 4000 and 6000, whereas in droplets larger than 30 μm , the Q-factor exceeds 10,000.

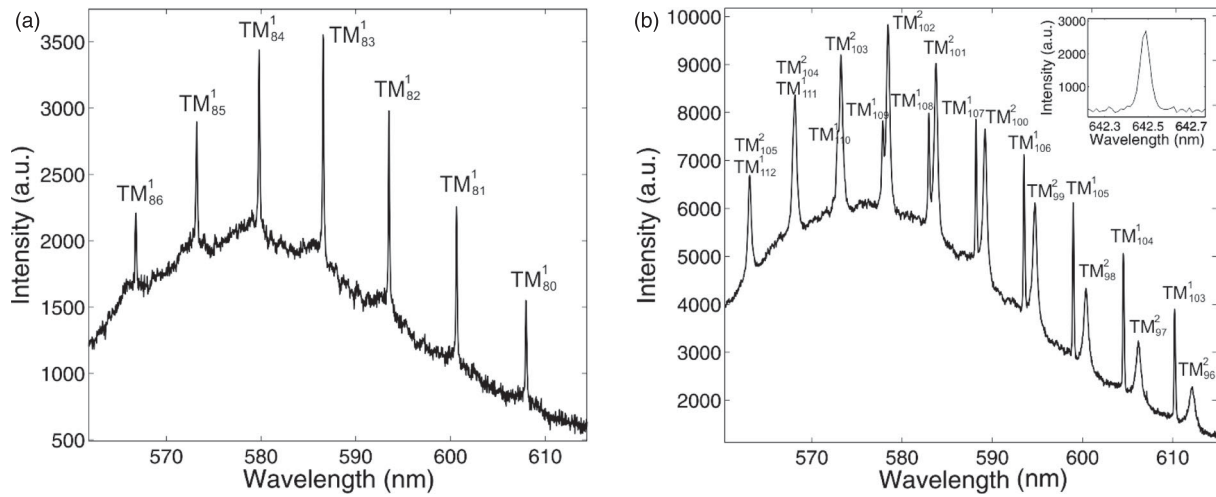


Figure 12. Spectrum of WGMs circulating in a liquid-crystal microdroplet. (a) A single set of WGM resonances is detected in smaller ($10\ \mu\text{m}$) droplets of a nematic liquid crystal in PDMS. The mode indices are assigned on the basis of the theory of WGMs in optically anisotropic microspheres. (b) In larger radial droplets ($12\ \mu\text{m}$), a second set of radial modes appears with a radial mode number $n = 2$. The inset shows details of a spectral WGM line in a $53\text{-}\mu\text{m}$ -diameter droplet. The linewidth corresponds to the cavity Q-factor of the order of 12,000 (reprinted by permission of Macmillan Publishers Ltd: Nature Photonics [67], copyright (2009)).

5. Tuning of WGM resonances by electric field, temperature and strain

Nematic liquid crystals are well known for their very large optical response to external fields, which is due to the minimisation of the electric energy of the induced electric dipoles in an external electric field. These optical effects are also well known from previous studies of PDLCs, in which a strong-enough external electric field forces the molecules inside the droplet to align nearly uniformly in the direction of the field. This results in index matching between the corresponding refractive index of the droplet and the external medium. We therefore expect that a strong-enough electric field will have a large impact on the WGM resonances. Figure 13 represents optical micrographs of a $9.3\text{-}\mu\text{m}$ droplet, as observed between the crossed polarisers, within an external field applied perpendicularly to the plane of the image.

A comparison of the images without and with the electric field (Figure 13(a) and 13(b)) clearly indicates the strong structural changes in the interior of the droplet when the electric field is applied. The schematic presentation of the evolution of the interior director structure is shown in Figure 13(c) and 13(d). At smaller fields, the centre of the droplets is affected in such a way that the radial hedgehog defect transforms into a ring-like structure (reference), which is pushed towards the interface of the droplet with an increasing field (Figure 13(d)). Finally, at very large fields, the whole interior of the droplet is aligned along the field direction, except for the topological ring defect itself and its

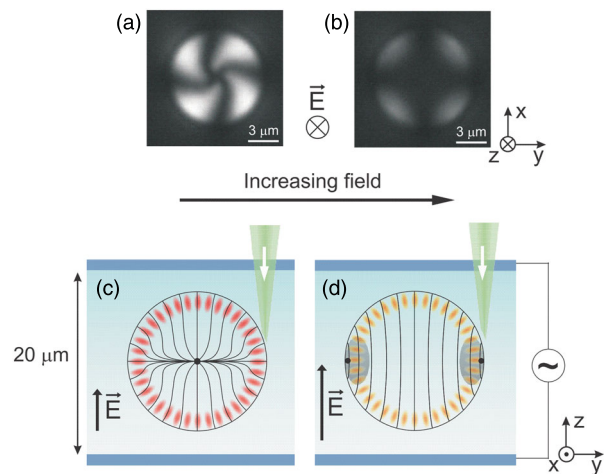


Figure 13. Effect of electric field on liquid-crystal microresonator. (a) A micrograph of a $9.3\text{-}\mu\text{m}$ droplet of E12 nematic liquid crystal in PDMS between the crossed polarisers at $1.9\ \text{V}_{\text{RMS}}\mu\text{m}^{-1}$ (b) The same droplet at $2.6\ \text{V}_{\text{RMS}}\mu\text{m}^{-1}$. Note the spontaneous twist of the radial structure in (a). (c,d) Schematic representation of the effect of an external electric field on the internal structure of radial nematic microdroplets. Reprinted by permission of Macmillan Publishers Ltd: Nature Photonics (reference [67]), copyright (2009).

immediate surroundings. It is easily understood from the observation of the mode distribution in Figure 13(c) and 13(d) that this structural deformation should shift the WGM resonances towards short wavelengths with increasing electric field. This is due to the reduced dielectric constant in the vicinity of the ring defect, which effectively shortens the optical path of the WGM resonant

wave. This means that the resonant condition will be fulfilled for shorter wavelengths.

This blue shift of the WGM resonances with increasing electric field is indeed observed in the experiments, as shown in Figure 14. At small electric fields, there is only a small electric-field-induced shift of the TM WGM resonances. When increasing the field, the wavelength shift decreases nearly linearly with an increasing electric field. There is no hysteresis in the WGM blue shift, which is also completely reversible. The response time is limited by the response dynamics of the nematic liquid crystal inside the droplet and is of the order of 10 milliseconds.

The electric-field-induced WGM shift depends on the diameter of the droplet and is as high as 20 nm at $2.6 \text{ V}_{\text{RMS}}\mu\text{m}^{-1}$ in $17\text{-}\mu\text{m}$ -diameter radial nematic microresonators, as shown in Figure 14(b). A theoretical estimate shows that the maximum tunability at a very high electric field is of the order of 6% or 40 nm at 600 nm.[67] The observed magnitude of the electric-field-induced shift of the WGM resonances in nematic microresonators exceeds similar phenomena in solid microresonators by at least one order of magnitude. In silicon-on-insulator ring resonators, the obtainable electric-field-induced shifts are less than one nanometre.[73] Electric-field-induced tuning of ring resonators is also achievable by adding a nematic liquid crystal as a cladding layer, and the WGM shift is obtained by tuning the dielectric constant of the evanescent wave close to (100 nm) the cladding-resonator interface. This results in larger tuning ranges of LC-cladded ring or racetrack microresonators. However, some authors report irreversible tuning.[76] In lithium niobate micro-ring resonators, the WGM shifts are less

than one nanometre at 300 V across a $200\text{-}\mu\text{m}$ gap.[77] By cladding a racetrack silicon microresonator with a dye-doped blue phase liquid crystals, tuning with laser light was obtained, with spectral shifts of the order of 1 nm.[78,79]

In all WGM microcavities, the mode resonances depend directly on the refractive index of the material, which in all cases is more or less temperature dependent. For solid-state micro-ring resonators the effect of temperature on the refractive index is small and, for example, a sensitivity of 10 pm/K at 1500 nm was achieved in silica.[80] In the case of soft materials such as PDMS, 0.3 nm/K at 1500 nm was shown.[81] Liquid crystals were employed previously for the temperature tuning of WGMs, but again just as a cladding. Temperature tuning of 8 nm at 1200 nm was also demonstrated.[76] It is well known that the refractive index of a liquid crystal is temperature dependent because of the degree of ordering of the liquid-crystal molecules. The degree of the orientational order is given by the order parameter S that is strongly temperature dependent and decreases when we approach the isotropic phase transition from below. We therefore expect that the WGM resonances will show a strong temperature dependence because of the temperature changes of the refractive indices.

The temperature dependence of the WGM spectrum of a E12 radial nematic liquid-crystal droplet is presented in Figure 15. We can easily identify three different sets of modes, which differ in respect to the radial mode numbers and polarisations. These modes, which are blue-shifted with increasing temperature, are all TM-polarised WGMs. There are two sets of modes

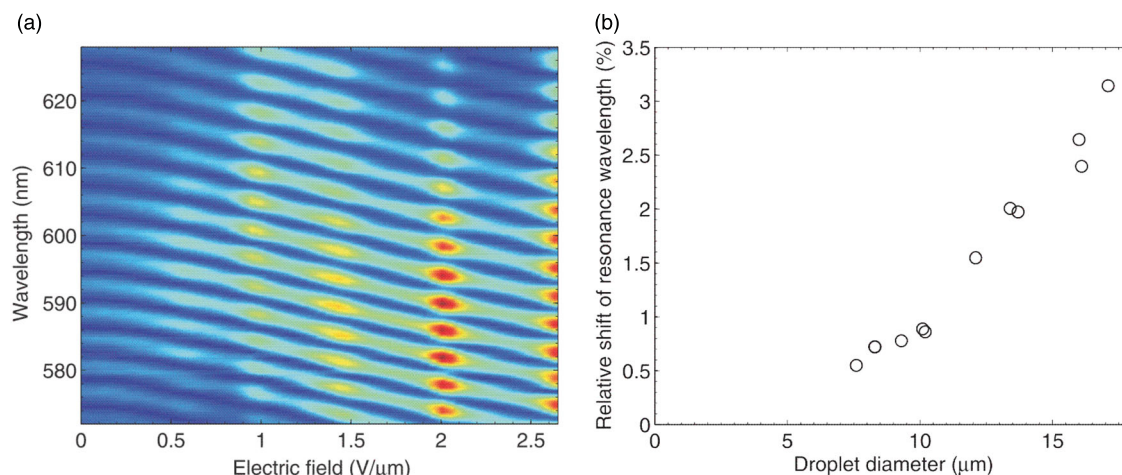


Figure 14. (a) Electric-field-induced shift of TM WGM resonances in a $16\text{-}\mu\text{m}$ microdroplet of E12 nematic liquid crystal. The colour scale indicates the intensity of the detected light. (b) Range of electric-field tunability of WGM resonances in radial E12 microdroplets. Reprinted by permission of Macmillan Publishers Ltd: Nature Photonics (reference [67]), copyright (2009).

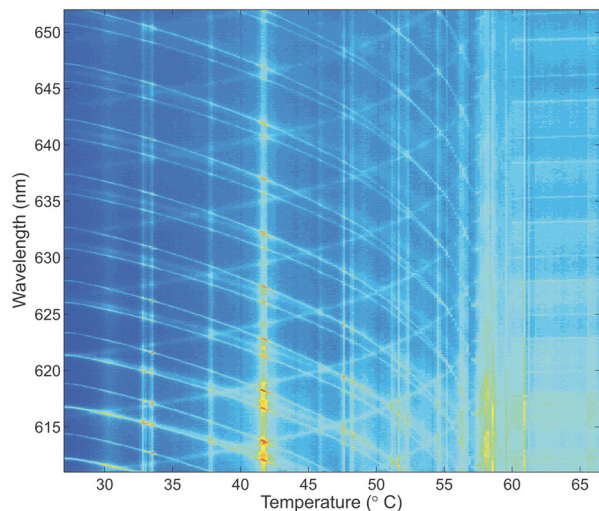


Figure 15. WGMs in a 23.1- μm -diameter droplet of a E12 in PDMS as the temperature is increased. The isotropic-nematic phase transition is at 57°C. Reprinted with permission, Copyright 2011 Society of Photo-Optical Instrumentation Engineers.

corresponding to $n = 1$ and $n = 2$. The third set of modes shows the opposite temperature dependence and is red-shifted with increasing temperature. At the phase-transition temperature, these modes merge into two sets of modes, which are temperature independent in the isotropic phase. The third set of modes obviously corresponds to the TE modes with their polarisation sensing the ordinary refractive index, which has the opposite temperature dependence compared to the extraordinary index.

The tuning of WGM resonators by mechanical deformation has been achieved in a number of different geometries and materials. Two examples are droplets of a liquid in a PDMS polymer [80,82] and fused-silica microresonators.[83] In both cases the achieved tunability was approximately 1 nm in visible light. When liquid-crystal microdroplets are embedded in an elastic polymer matrix, such as the PDMS, the film can be mechanically stretched, and the spherical droplets deform into an ellipsoid, as shown in Figure 16. When the droplet is illuminated near its rim, we can clearly observe the circulation of the WGMs inside the deformed droplet. Figure 16 shows the strain dependence of the WGM resonances, up to the maximum applied strain of 15%. The modes are red-shifted, which indicates that the optical path of the resonant modes increases with the increasing strain. This is understandable because of the ellipsoidal deformation of the droplet and the fact that the light is circulating in the plane containing the larger axis of the ellipsoid. The strain-induced red-shift is rather dramatic and is of the order of 10 nm at 5% strain.

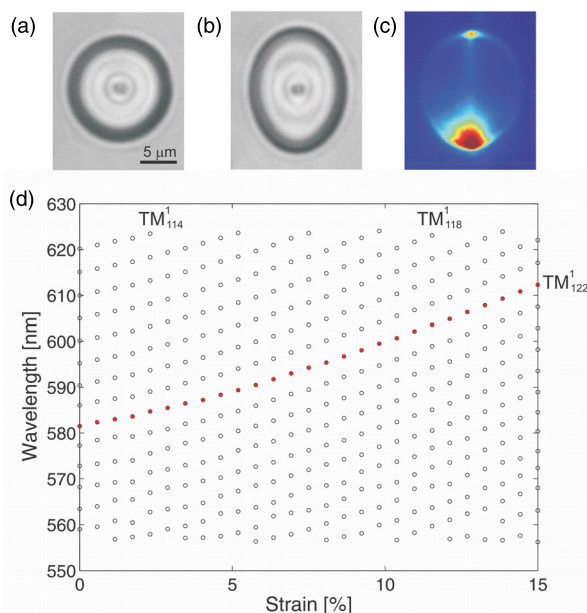


Figure 16. (a) A liquid-crystal droplet with 14.4- μm diameter embedded in PDMS at 0% strain and (b) at 15% strain. (c) Fluorescent intensity at 7.4% strain. The droplet is illuminated by a focused laser near its rim at the lower part of the image. (d) Strain dependence of the WGM resonances, measured for the same droplet. Reprinted with permission, Copyright 2011 Society of Photo-Optical Instrumentation Engineers.

6. Surfactant sensing based on WGM lasing in liquid-crystal microdroplets

The alignment of liquid-crystal molecules at the interface with the external medium depends in a complicated way on the inter-molecular interactions across the interface. Because the surface anchoring of liquid-crystal molecules depends on the chemical constitution of the interface, these interfaces have been used successfully to detect foreign molecules and objects that are attached to this interface from the external medium. For example, phospholipids at the liquid-crystal water interface were detected via polarised-optical-microscope observations of small compartments filled with liquid crystal, having one free interface with an external water reservoir. The same optical method of observing the changes in birefringence was used to detect proteins, viruses, and bacteria, which preferentially attached to the liquid-crystal water interface and modified the surface boundary conditions for liquid-crystal molecules. This change of the interfacial anchoring of the liquid crystal propagates into the interior of the liquid crystal and therefore induces huge structural changes. These structural changes are accompanied by large changes in the optical properties of the liquid crystal, which strongly amplifies the surface effects. The surface sensitivity of a liquid crystal to external agents represents a novel concept for a sensor

device in which tiny changes at the interface induce large structural changes in the interior of the sensor, therefore providing a strong response to a very small number of molecules attached to the interface.

It has been demonstrated in the past that liquid-crystal interfaces are a superior sensing platform for the detection of foreign molecules in a water environment that is in contact with a liquid crystal.[84–86] However, the main drawback of this method is a rather impractical optical readout, which uses optical microscopy and pattern recognition by the observer to detect the change in the structure of the sensor. One way to overcome this difficulty is to make a small droplet of liquid crystal, which floats in an aqueous environment, to detect the presence of foreign molecules in water or some other external medium. As the surface boundary condition changes after the surface adsorption of the targeted molecules at the liquid-crystal/external interface, the interior structure of the droplet may change. This change can be detected by measuring the spectrum of WGM resonances inside the droplet. The monitoring of WGM spectra in liquid-crystal microdroplets could therefore be used as a versatile platform for the contactless and simple optical detection of small concentrations of targeted molecules in water.

A typical experiment demonstrating the sensitivity of WGM resonances to foreign molecules dispersed in water is performed by using nematic liquid-crystal microdroplets doped with a small amount of fluorescent dye, which serves as a uniformly distributed light emitter. The microdroplets are produced by mechanically mixing some microlitres of dye-doped 5CB in one millilitre of 4-mM water solution of sodium dodecyl sulphate (SDS). For this concentration of SDS, the 5CB droplets obtain a radial distribution of liquid-crystal molecules. The SDS also prevents the droplets from sticking to the walls of the microfluidic channels used in the experiment. The dispersion of 5CB droplets in a 4-mM SDS water solution is introduced into the microfluidic channel positioned in the operating field of the laser tweezers. A selected droplet of 5CB can be trapped with an infrared laser tweezer because of the higher refractive indices of the 5CB compared to water. After trapping the droplet, a continuous flow of pure water is fed through the channel so that the SDS concentration is reduced to zero. This flow of purified water flushes most droplets out of the channels, except for the trapped ones. Simultaneously, the internal configuration of the director field changes from a radial to a bipolar configuration, which is stable for a zero concentration of SDS.

After purifying the channels with water, the droplet is exposed to a continuously increasing concentration of SDS, which is fed through the main channel. The

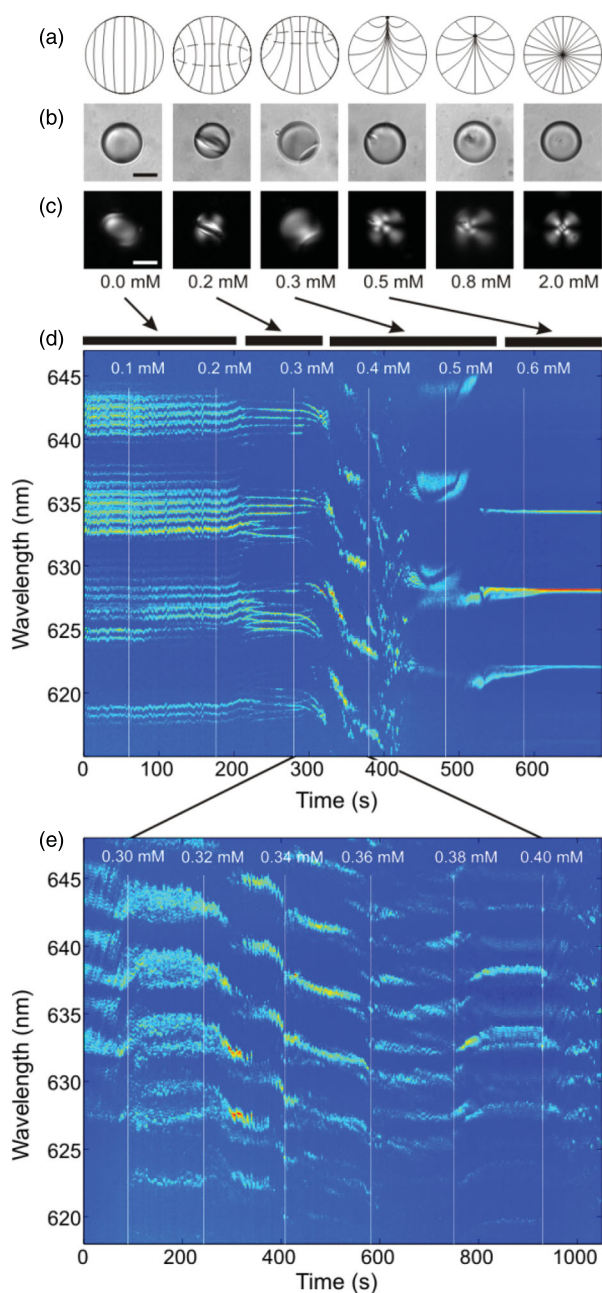


Figure 17. Changes to the structure of a small droplet of nematic liquid crystal at increasing concentrations of SDS. (a) The schematics of the director field, represented by the lines, where the dots are point defects. The structure changes from bipolar at zero SDS concentration, with the two boojums located outside the droplet, to the radial configuration, which emerges at 2.0-mM SDS. (b) Unpolarised microscope images of a 17- μm -diameter microdroplet of 5CB in water with added SDS. The “inner ring” at 0.2-mM of SDS is clearly seen. The $+1/2$ ring defect evolves into a point radial defect with a charge $+1$. This point moves gradually from the interface into the centre and establishes the radial configuration of the droplet. (c) The same images as in (b), but taken between crossed polarisers. (d) The spectrum of light emitted from a 13- μm 5CB droplet in water with various concentrations of SDS. (e) Close-up of a part of the lasing spectrum at the intermediate SDS concentrations, where the structure of the droplet is not very well defined. Image courtesy M. Humar.

response of the WGM microlaser to this continuously changing concentration of SDS in the water is shown in Figure 17. The lasing spectrum changes dramatically when the interior of the droplet is transformed into the bipolar configuration above a 0.5-mM concentration of SDS, as shown in Figure 17. Instead of a set of practically equidistant modes, we can clearly observe several groups of WGMs. Within each group, the modes are split by an order of 0.5 nm and the width of the lasing lines is typically 0.05 nm, which is limited by the spectrometer resolution. This mode splitting is typical of WGM microcavities, which have a non-uniform refractive-index distribution. Namely, if the spherical WGM microcavity is filled with an isotropically or radially uniform refractive index, the WGM modes with different azimuthal mode numbers are degenerate. However, as soon as the optical path is different in different planes of light circulation, these modes split. The mode splitting can either be a consequence of the droplet's deformation to a non-spherical shape, or a consequence of a slightly different refractive-indices distribution in different planes of circulation. Because the optical microscopy confirms the spherical shape of the droplets with the bipolar internal organisation, the mode splitting can only be explained by the refractive index's spatial non-uniformity. Indeed, in bipolar droplets with the two point defects located exactly at the interface, all the orbits of light circulation very close to the interface have the same optical path. However, the difference in the optical paths emerges as soon as the two point defects (boojums) are located outside the droplet.

7. 3D microlasers from cholesteric liquid crystals

In 2010, Humar and Mušević demonstrated a compact and self-assembled microlaser based on cholesteric liquid crystals.[68] To do this, they mixed a liquid crystal with a non-miscible fluid, such as glycerol or PDMS. Due to the chemical incompatibility, tiny droplets of cholesteric liquid crystal were formed in the carrier fluid, and because of the surface tension, the droplets obtained a perfect spherical shape. Due to the parallel anchoring of the liquid-crystal molecules at the interface with the external fluid, these microdroplets organised their cholesteric interior with the helical axis pointing from the surface to the centre of the droplet at all points of the droplet's surface. This spontaneous self-assembly, which occurs solely due to the helical nature of the cholesteric liquid crystal and the surface anchoring, results in an optical structure, shown schematically in Figure 18.

Cholesteric microdroplets with degenerate planar-surface anchoring have been studied before, but in contexts other than their application as spherical optical

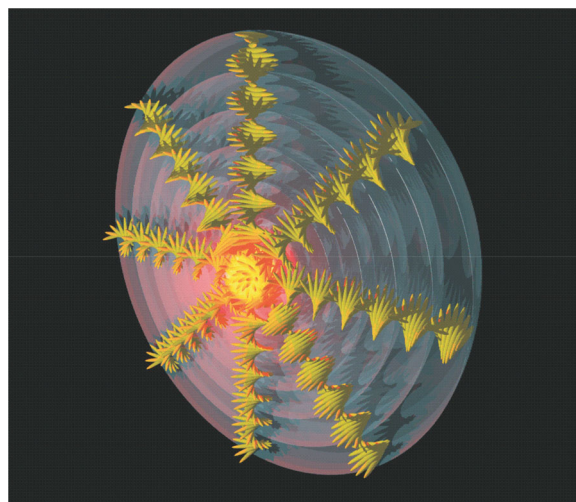


Figure 18. Schematic view of the arrangement of molecules in a cholesteric liquid-crystal microdroplet with parallel anchoring of the liquid-crystal molecules at the surface. The helical structure of the liquid crystal originates from the centre of the droplet and gives rise to a series of concentric shells of constant refractive index. This dielectric structure is optically equivalent to the well-known Bragg-onion optical microcavity. Image courtesy of M. Humar.

microcavities. In the experiments,[87–89] most commonly it was the radial spherical structure that was observed,[90] also known as the spherulitic texture or the Frank-Pryce model.[91] In this structure, there are no singular defects and a twisted cholesteric disclination winds out from the centre of the droplet to the surface. There are theoretical predictions about the existence of two other cholesteric structures [92,93]: the diametrical spherical structure, and the planar bipolar structure.

Spherical Bragg-onion microcavities, which are based on an alternating sequence of concentric shells of low- and high-refractive-index material, are particularly interesting because of their perfect rotational symmetry in 3D, which means that the photonic band gap has to be independent of the direction of light propagation. It is therefore expected that a DFB laser based on a cholesteric microdroplet would emit laser light uniformly in all directions, and that the light would be circularly polarised in view of the helicity of the birefringent structure.

A cholesteric liquid-crystal 3D microlaser is made by mixing a low-birefringent liquid crystal (such as the MLC-7023 liquid crystal produced by Merck) with a chiral dopant (such as S-811). This produces a chiral nematic liquid crystal with a helical period and a photonic band gap (PBG) in the visible part of the spectrum. The period of this mixture and its ordinary and extraordinary refractive indices completely determine the lasing wavelength. In order to match the emission spectrum of

the fluorescent gain medium to the photonic band gap (PBG), a proper dye has to be selected. Typically, 0.2 wt.% of the fluorescent dye Nile red or DCM is used. These dyes are then optically pumped using a doubled Nd-YAG pulsed laser, the driving frequency of which is several tens of Hertz.

After the mixture of chiral nematic liquid crystal and dye is thoroughly homogenised at elevated temperatures, it is cooled down and mixed into glycerol by hand. This process instantaneously produces millions of tiny cholesteric liquid-crystal microdroplets. They are of different diameters, but the PBG of all these droplets is the same because they are made of the same material. Such a simple process thus creates a myriad of dye microlasers that all emit exactly the same wavelength. An example of a cholesteric microdroplet with a somewhat larger helical pitch is shown in Figure 19(a) and 19(b). In this material, the amount of chiral dopant was deliberately lowered, so that the helical pitch increased to a length that could be easily observed under an optical microscope.

Figure 19 (d)–(f) shows selected video frames of a cholesteric droplet with a PBG in the visible spectrum,

which is optically pumped with gradually increasing power. Below the threshold for lasing, the droplet is emitting uniformly fluorescent light (orange in this case) with a broad spectrum. By increasing the optical pump power, we eventually reach the threshold for lasing, where the gain due to the stimulated emission is higher than the optical losses from the cavity. This results in the appearance of a tiny bright spot in the centre of the droplet. By further increasing the power of the optical pump, this tiny spot is enlarged, but still confined to the centre of the droplet. If we change the direction of the observation, the image of the droplet remains the same – we always see a bright spot at the centre of the droplet, irrespective of the direction of observation. There is an obvious conclusion to be drawn from this experiment: the cholesteric droplet is a 3D Bragg-onion microlaser that emits coherent light from its centre. Such a droplet is therefore a point source of monochromatic and coherent light.

The spectral properties of the emitted light below and above the threshold for lasing are shown in Figure 20(a)–(d). Figure 13(a) shows a series of optical spectra of emitted light for various and increasing energy

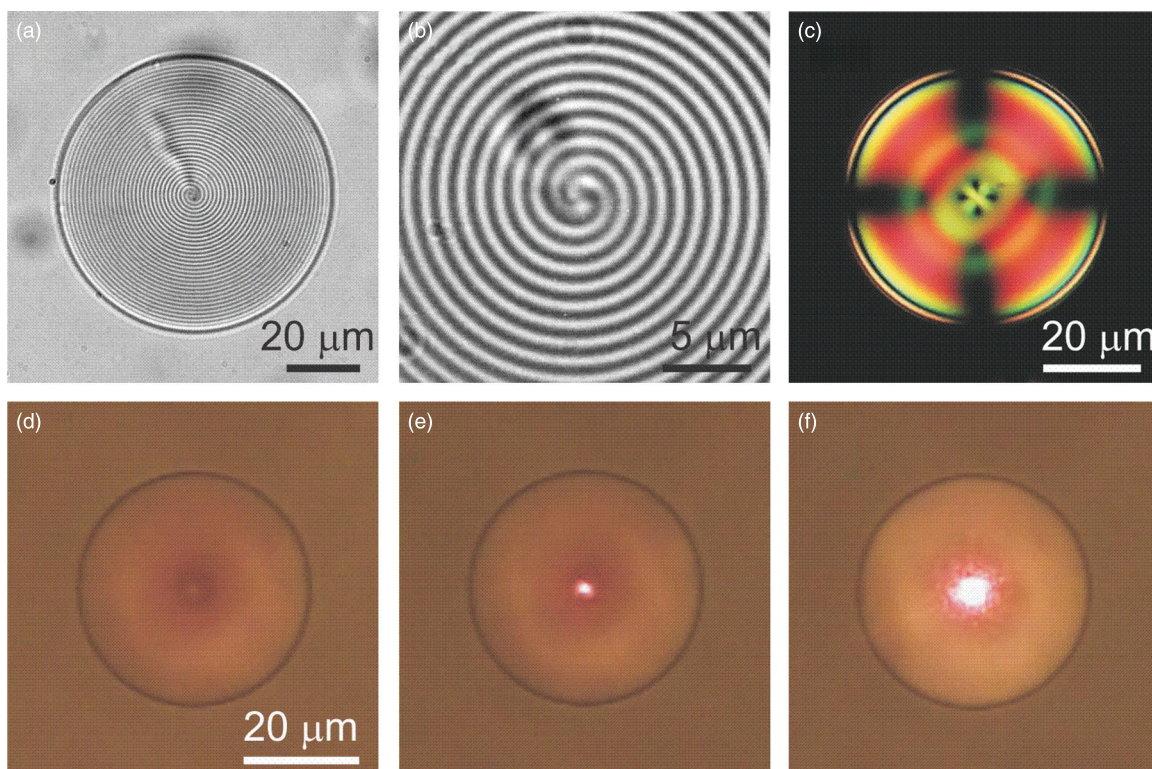


Figure 19. (a) A typical cholesteric droplet with a pitch $p = 2.2 \mu\text{m}$ in glycerol. The light and dark concentric shells are a result of the spatial variation of the refractive index of the cholesteric liquid crystal in the radial direction. A blurred defect line can be seen extending from the centre to the surface. (b) Close-up of the centre of the cholesteric droplet, when viewed along the defect line. (c) Cholesteric droplet with PBG in the visible range of light viewed under crossed polarisers and white-light illumination. (d)–(f) Omni-directional (3D) lasing from a cholesteric droplet illuminated by laser pulsers and a weak, white, background illumination. (d) Below the lasing threshold, the droplet is fluorescing uniformly. (e) At the threshold for lasing, a bright spot of radiating monochromatic light is emerging from the centre of the droplet. (f) Lasing is very intense at a high optical pump power. Image courtesy of M. Humar. Reprinted with permission of Optical Society of America, Ref. [68].

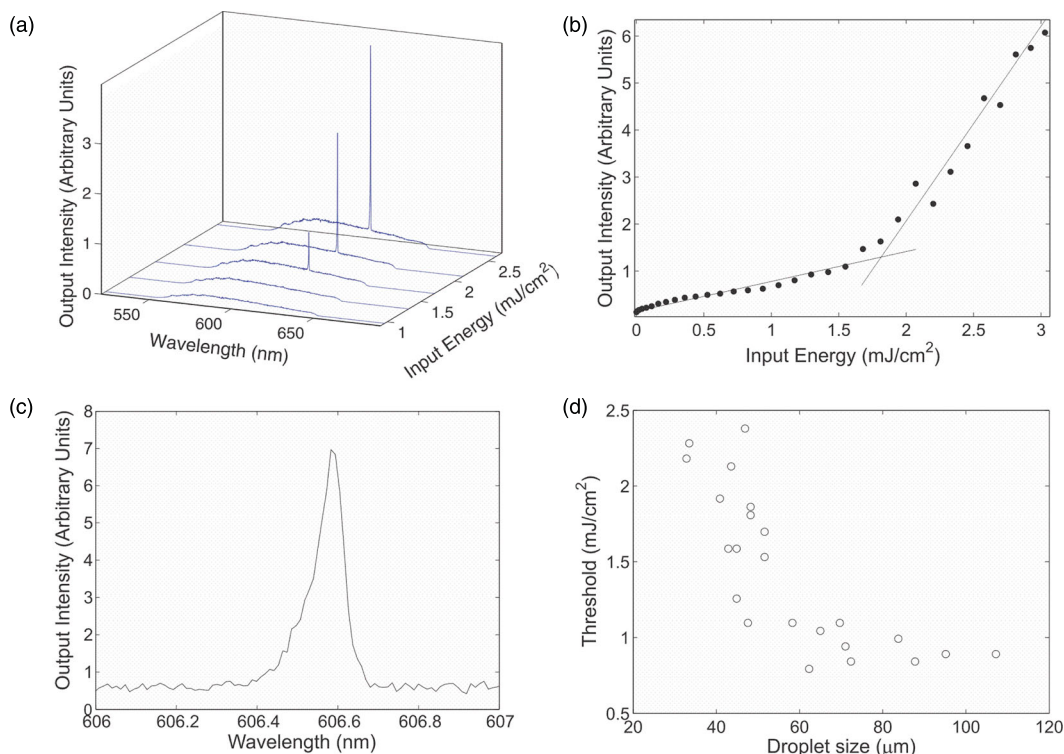


Figure 20. Lasing characteristics of a single droplet of dye-doped cholesteric liquid crystal. (a) The spectra of light emitted from the centre of the microdroplet at different energies of the pumping pulse. (b) Radiated laser-light intensity as a function of the input pulse energy density. There is a clear threshold for lasing. (c) Magnified lasing spectrum showing a laser linewidth of 0.1 nm. (d) The threshold for lasing as a function of the droplet size. For this material, there is no lasing in the droplets with diameters smaller than 30 μm . Reprinted with permission of Optical Society of America, Ref. [68].

densities of the optical pump light. Below the threshold, only a fluorescent background spectrum of Nile red is observed. At the threshold of about $1.5 \text{ mJ}/\text{cm}^2$, a sharp spectral line emerges from the fluorescent background, and is strongly amplified by increasing the optical pump power density. Clearly, the optical mode of the chiral microcavity is amplified and picked up, so that it becomes a lasing mode. Importantly, this is a single-mode laser, as no other modes of the cavity are amplified above the threshold for lasing.

The threshold power for 3D lasing depends on the droplet diameter and the birefringence of the cholesteric liquid crystal. Materials with lower birefringence have a higher threshold because the strength of the radial modulation of the refractive index is not as high. Correspondingly, the grating in the radial direction does not have a large amplitude and the optical losses are high. This increases the threshold for lasing in the low-birefringent cholesteric microlaser. If we take a high-birefringent liquid crystal, the radial variation of the refractive index has a large amplitude and the losses of the resonator are lowered. This lowers the threshold for 3D lasing, but causes another complication, i.e., the emergence of other modes. Typically, these are WGMs, which combine with the 3D

mode and give rise to a complex lasing pattern, as shown in Figure 21.

The spectral width of the 3D emitted laser line is relatively narrow, as shown in Figure 20(c). Typically, the linewidth is of the order of 0.1 nm. Other characteristics of the 3D microlaser include circular polarisation of the emitted light, uniform distribution of the emitted light in 3D and the possibility of tuning the emitted wavelength via the temperature of the external field.

There have been several other experiments on the optical properties of chiral nematic microdroplets with planar surface anchoring. It was demonstrated that dispersions of chiral microdroplets could be used as a sort of “laser paint”, [94] which could be applied to the surface and subsequently dried. After the evaporation of the carrier fluid, the droplets were pressed against the surface by the surface tension of the evaporating fluid. This resulted in a thin layer of flattened, pancake-like microdroplets, distributed on the surface with their helical period oriented perpendicularly to the surface. Upon optical pumping, this layer of pancake-like microlasers emitted laser light. It was demonstrated in other experiments that cholesteric microdroplets could be successfully polymerised, leading to a stable photonic

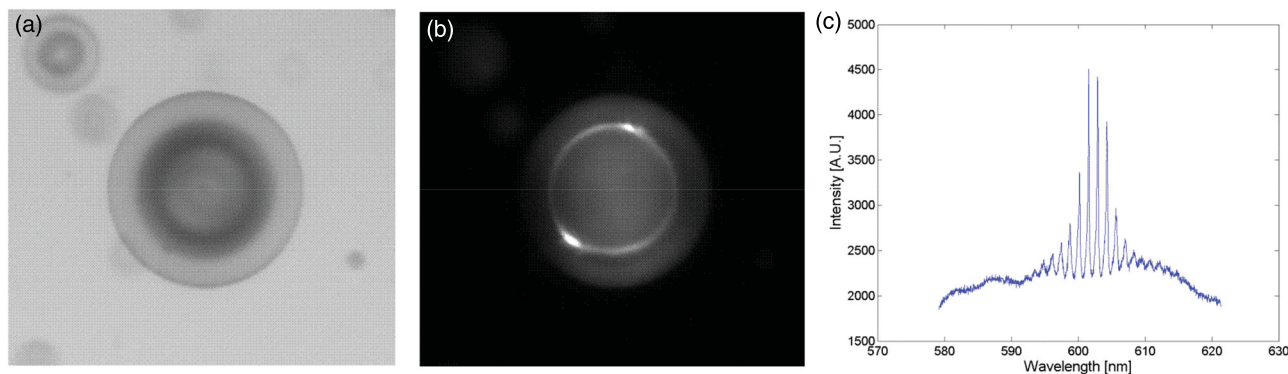


Figure 21. Lasing from a high-birefringent cholesteric microdroplet with a slightly longer pitch exhibits a mixture of 3D and whispering-gallery lasing modes. Image courtesy of M. Humar.

microcavity [95] into which fluorescent dyes could be added. There are interesting laser-trapping experiments with polymerised chiral nematic microdroplets, which act as chiral colloidal particles. Because of the PBG, such a chiral particle selectively reflects the rather narrow frequency band of circularly polarised light, whereas other wavelengths and oppositely handed circularly polarised light are transmitted. As a result, such a chiral colloidal particle can be selectively trapped or repelled from the laser beam.[96,97]

8. Optical microfibres from smectic-a liquid crystals

While in spherical objects the surface energy of the liquid crystal in the carrier fluid dominates the elastic energy of its deformed interior, lowering the surface energy could result in the formation of elongated, fibre-like objects. This is in fact well known for diblock polymers,[98] where elongated, fibre-like objects called “myelin figures” are familiar. The process of the spontaneous formation of myelin figures is also well known for the interface of lyotropic lamellar liquid crystals and water.[99] Similar objects were reported by Prathiba et al. [100] in binary mixtures of liquid crystals. It was demonstrated recently that the thermotropic smectic-A liquid-crystal 8CB forms micrometre-diameter filaments when dispersed in water with added CTAB.[101]

Myelin figures are tube-like structures consisting of cylindrically bent water/surfactant bilayers. The Myelin figures are clearly some sort of liquid optical fibres; however, the small difference between the refractive index of the myelin fibres and their aqueous environment renders them unsuitable for wave-guiding applications. A recent demonstration of the spontaneous formation of myelin-like structures grown at the interface of a thermotropic smectic-A liquid crystal and water containing cationic surfactant micelles triggered an interest in the photonic

properties of these structures. The reason for this is as follows: (i) The coaxial organisation of smectic layers in the myelin fibres could result in a very precise and uniform diameter of the fibres to one molecular length (2–3 nm); (ii) The smectic nature of these fibres should substantially decrease the degree of light-scattering losses and surface smoothness. This is because molecular orientational fluctuations are suppressed in the smectic-A phase; (iii) The coaxial smectic-A fibre should have a topological line defect of the winding number + 1 along the major axis of the tube. This line defect must be in perfect alignment with the cylindrical axis of the fibre. It is expected that the optical modes of such a birefringent fibre with a topological line defect should support the eigenmodes of the electromagnetic field, which exhibit topological similarities and are carrying the topological charge.

It was demonstrated recently that these smectic-A liquid-crystal fibres, grown from the interface of water and CTAB, are excellent optical waveguides, where not only guiding but also lasing was demonstrated.[102] In the experiment, a common, room-temperature smectic-A liquid-crystal 8CB is used. This material is normally labelled with a small amount of fluorescent dye, such as Nile red, which helps us trace the propagated light under an optical microscope. For the preparation of the aqueous solution, a cationic surfactant is used, such as C16TAB. The critical micellar concentration of this surfactant in water is around 1 mM at 25°C. However, in the experiments, much higher concentrations are used, typically between 10 and 100 mM. After a small amount of 8CB-dye mixture is put on a glass substrate, it is covered with a second glass plate and the aqueous micellar solution of CTAB is brought into contact with the liquid crystal using capillary forces. Under an optical microscope, we can immediately see very fine microtubes protruding from the liquid-crystal/aqueous interface into the aqueous phase. An example of this fibre-like phase is shown in Figure 22.

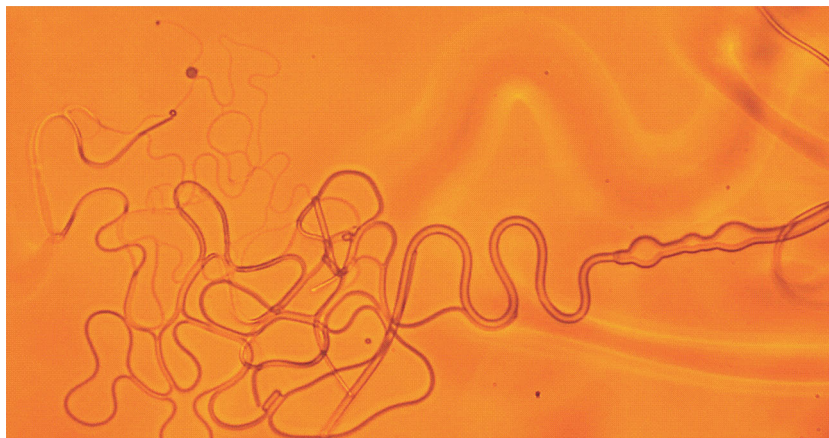


Figure 22. Microscope image of 8CB microfibres grown in a water solution of CTAB. The structures are far from being at equilibrium – we can see the vivid motion, growth and shape-changing dynamics of these microfibres for several minutes. Occasionally, after the CTAB is consumed, the fibres contract back into spherical-like isolated objects or clusters. Copyright 2015 Society of Photo-Optical Instrumentation Engineers.

To investigate the interior organisation, we used an optical polarising microscope and a fluorescence confocal polarising microscope (FCPM). When viewed between crossed polarisers, 8CB microfibres exhibit typical birefringent colours, as illustrated in Figure 23(a). The birefringent layers run along the long axis of the fibre, which has a perfectly spherical microcap at both ends. The strength of the surface tension between the 8CB and

the aqueous environment makes the interfaces extremely smooth. For example, the spherical cap always preserves its shape, regardless of the bending and twisting of the 8CB microfibre.

If the fibre is rotated between crossed polarisers, it becomes dark when the axis of the fibre is either parallel or perpendicular to the polarisation of the light. This indicates that the fibre is structurally homogeneous, that

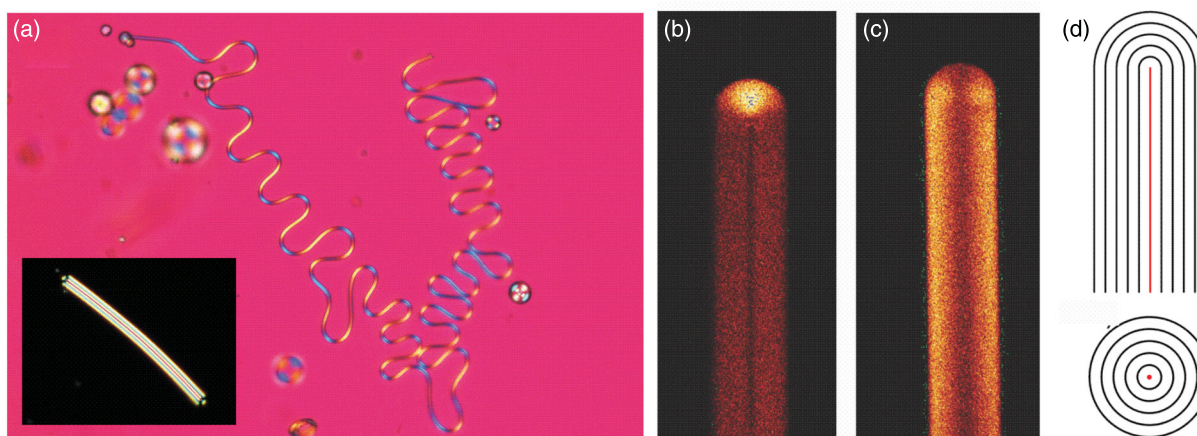


Figure 23. Polarising microscopy and FCPM images of smectic-A 8CB microfibres (doped with 0.01 wt.% of Nile red) in aqueous C16TAB solution. (a) A thin 8CB fibre (diameter $\approx 3 \mu\text{m}$), which has adopted a bent, S-like shape between the crossed polarisers with the addition of a red (λ) wave plate. The alternating yellow/blue colour sequence indicates that the liquid-crystal molecules, and thus the local optical axis, are always aligned perpendicularly to the surface of the fibre. The inset shows an 8CB microfibre (diameter $\approx 10 \mu\text{m}$) between crossed polarisers, demonstrating a strong birefringence of the smectic fibre. (b) FCPM image of a smectic-A 8CB microfibre (diameter $35 \mu\text{m}$) with the polarisation of the exciting light along the axis of the microfibre. A high fluorescence intensity is observed at the spherical tip of the fibre. (c) FCPM image of the same fibre with the polarisation of the exciting light perpendicular to the axis of the microfibre. A high fluorescence intensity is observed along the cylindrical body of the fibre. The distribution of the fluorescence intensities in both images indicates that the Nile-red molecules, and thus the liquid-crystal molecules, are oriented perpendicularly to the surface of the fibre. (d) Schematic drawings of the coaxial arrangement of smectic layers in the microfibre. Top: cross-section parallel to the fibre axis. Bottom: cross-section perpendicular to the fibre axis. The red line and the dot indicate the topological line defect. The rod-like liquid-crystal molecules (not shown in the drawings) are oriented perpendicularly to the layer planes and the fibre surface. Image courtesy of K. Peddireddy.

the optical axis of the smectic-A liquid crystal is oriented perpendicularly to the surfaces of the fibre and that it ends at the topological line defect in the centre of the crystal. This is confirmed by taking FCPM images of the fluorescently labelled fibre. When using the Nile-red dye for fluorescent labelling, we know that the Nile-red molecules align within the 8CB liquid-crystal matrix with their radiative dipole moments along the local director. This means that the fluorescence is the most intense when the polarisation of the excitation light is parallel to the Nile-red molecules and therefore parallel to the director. By taking FCPM images across the whole volume of the fibre, we can determine the internal organisation of the fibre with absolute certainty.

FCPM images for two different polarisations of the excitation light are shown in Figure 23(b) and 23(c). When the polarisation of the excitation light is parallel to the axis of the fibre (as in Figure 23(b)), fluorescent light is collected only from a small part of the fibre's cap. In this case, the most intense light comes from the central part of the cap, which indicates that in this part the molecules are locally oriented along the axis of the fibre and are perpendicular to this direction in other parts of the fibre. When the polarisation of the excitation light is rotated by 90° , the fluorescent image of the fibre looks inverted compared to the previous one, as shown in Figure 23(c). Again, the most intense parts of the image indicate a molecular alignment perpendicular to the axis of the fibre. The combination of both images for two different polarisations provides a clear conclusion regarding the structure of the fibre, which is illustrated in Figure 23(d). Each fibre is composed of a sequence of coaxial and rolled-up smectic-A layers, which form the body of the fibre, and of two hemispherical caps at each end of the fibre. Inside these caps, the smectic layers form a sequence of nested hemispherical molecular layers. All the nested layers together form a highly birefringent and perfectly hemispherical lens with no topological defects. However, there must be a topological line defect in the core of the fibre, running all along the length of the fibre and connecting the centres of the two hemispherical caps.

An interesting issue is related to this topological defect line in the core of the fibre – having a topological line defect in their core, these microfibres are likely to support Gaussian-Laguerre eigenwaves. As demonstrated recently,[103] a Gaussian beam is transformed into a Laguerre-Gaussian beam after passing through a microdroplet of nematic liquid crystal with a topological point defect in the centre. A similar transfer of phase singularity from the material field to the light was reported for arrays of umbilic topological defects in liquid crystals [104] and defects in toron gratings.[105] The experiments show that the topological defects of the matter are

expected to be transferred and imprinted into the electromagnetic waves as phase singularities. Furthermore, the perfectly hemispherical caps of the smectic-A fibres could act as perfect self-assembled hemispherical lenses, collecting the light from the exterior.

9. Waveguiding and lasing in smectic-a microfibres

Perfectly ordered smectic fibres of micrometre diameter are good candidates for the waveguiding of light. The smectic-A liquid crystal is organised so that the local optical axis is pointing radially outwards from the centre of the fibre, which indicates that guided light experiences an effective refractive index close to the extraordinary index of refraction of the smectic material. For thermotropic smectics, such as 8CB, it is much higher ($n = 1.7$) than that of water ($n = 1.33$). To observe the waveguiding of light along smectic fibres, a special technique is used where the interior of the fibre is labelled with a fluorescent dye. When the short-wavelength light is guided along the fibre, it excites the fluorescence of the dye molecules, and this fluorescent light is partially emitted from the fibre. An example of a microscope image of a smectic-A fibre that was fluorescently doped with Nile red is shown in Figure 24. A strongly focused beam from the Ar^+ is positioned so that it illuminates one point on the fibre. Fluorescently generated light is emitted in all directions from this point, and a certain portion of the light is waveguided along the fibre because of the total internal reflection at the interface. As the light is propagating along the fibre, it excites fluorescent molecules, which again emit light in all directions. This means that under an optical microscope, we can see the fluorescently emitted light from those parts of the fibre where waveguiding occurs.

In addition to the observed waveguiding of light along a smectic-A fibre, another optical phenomenon is observed, when the fibre is illuminated with strong laser pulses that can excite the fluorescent molecules, as shown in Figure 25. At a low intensity of the excitation light, we can observe the emission of fluorescent light from the illuminated area. The spectrum of this light is rather broad. However, when the intensity of the excitation light is increased, bright lines are observed on the surface of the fibre at some point. In addition to the brightness, these lines show characteristic speckles, which indicate the coherent nature of the emitted light. We should stress that the bright lines indicate the emission of coherent and monochromatic laser light in a direction tangential to the surface of the fibre.

The observed lasing originates from the resonant WGMs of light, where the light is circulating along the

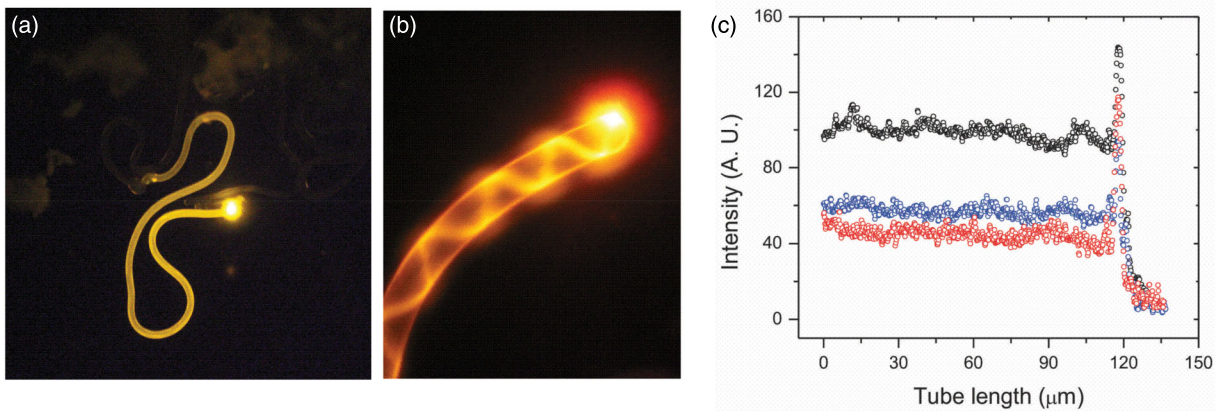


Figure 24. (a) Optical microscope image of a smectic-A fibre from 8CB, doped with Nile red and illuminated with a focused Ar^+ beam. Light is guided along the fibre due to the total internal reflection at the interface. (b) Details of waveguiding due to total internal reflection are clearly seen in the thicker fibre. The light beam from the illuminated spot on the cap of the fibre is spiralling along the fibre by total internal reflection. (c) Optical losses in smectic-A fibres are low. The chart shows the measured fluorescent intensity as a function of the position along the smectic-A fibre. There is little decrease in the intensity of the light along the 120 μm path. Image courtesy of K. Peddireddy.

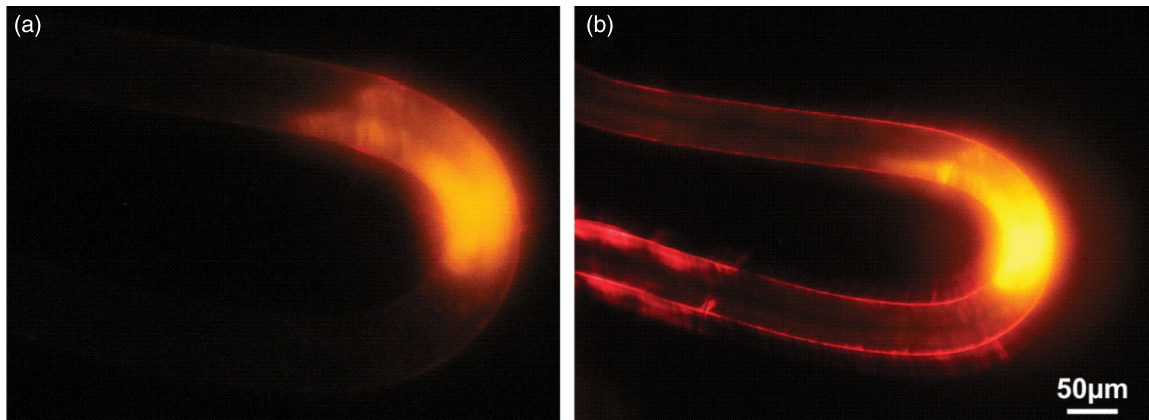


Figure 25. An example of lasing from a large, 50- μm -diameter smectic-A microfibre. The fibre is grown from Nile-red-doped 8CB in contact with a 100-mM C16TAB water solution and illuminated with a focused Ar^+ beam. (a) Below the threshold for lasing only a broad fluorescence spectrum from the illuminated area of the fibre is observed. (b) Above the threshold for lasing, we can clearly see a thin red line of strong intensity along the surface of the fibre. The monochromatic colour of the line indicates lasing. A close-up of the lasing line shows the characteristic laser speckles, indicating the coherence of the light. Image courtesy of K. Peddireddy.

perimeter of the microfibre because of the total internal reflection at the 8CB-aqueous interface. In WGM resonators, the resonant condition is achieved by light circulation along the circumference of the cavity, such as microsphere, microtoroid, microfibre. Because of the total internal reflection, the WGM cavities exhibit large Q-factors, enabling low-threshold lasing with a very small mode volume. In this case, the laser light is emitted from a resonator in the plane containing the circular path of resonant light and bounces off the cavity's interface due to total internal reflection. When such WGM lasing is observed under a microscope, we can usually see a strong coherent light shining towards the observer from the thin interfacial region of the cavity.

In the case of smectic-A fibres, we have a high-refractive-index fibre with a circular cross-section, which represents a cylindrical microresonator. The WGMs are resonantly circulated by total internal reflection in a plane that is perpendicular to the axis of the cylindrical cavity (i.e., the fibre's axis). In this case, the WGM lasing can be seen as a thin “sheet of light” emanating from the interface, as shown in Figure 25(b). The same picture is seen from all angles of observation due to the cylindrical symmetry of the resonator.

The spectrum of light emitted from the fibre is shown in Figure 26(a) and 26(b) for various levels of pumping light. Just at the threshold of lasing, we can see laser lines emanating from a broad fluorescent background. Well

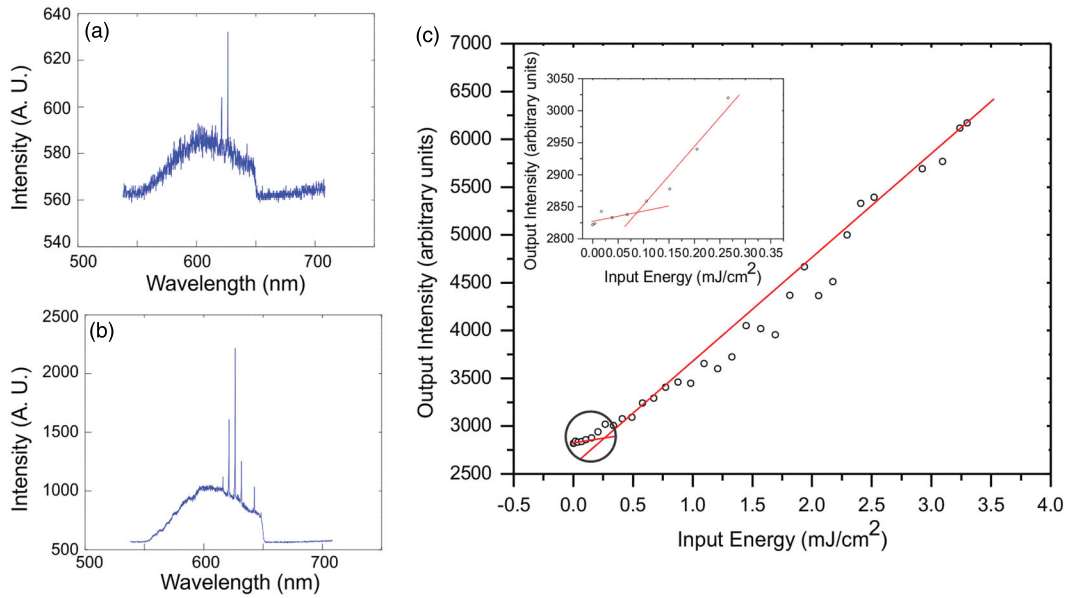


Figure 26. WGM lasing from a Nile-red-dye-doped smectic-A microfibre of 8CB in a 100-mM C16TAB water solution. (a) The lasing spectrum just above the threshold for lasing. (b) The lasing spectrum well above the threshold. (c) The intensity of the emitted spectral line as a function of the laser excitation energy. The inset shows an enlarged part of the diagram close to the threshold for lasing. Reprinted with permission of Optical Society of America, Ref. [102].

above the threshold, the lines are much stronger than the background fluorescence. The structure of the lines can clearly be attributed to the WGM spectra of the cavity with a circular cross-section. The lasing shows a low threshold and occurs at the exceptionally low value of $75 \mu\text{J}/\text{cm}^2$, indicating a high Q-factor for the smectic-A fibres.

10. Resonant transport of light in microphotonic circuits

In electronic circuits, the transport of electrons between different elements is achieved simply by establishing an electrical contact between the electrically conducting elements. In photonic circuits, different photonic elements are connected in a similar way, i.e., by joining the confining surfaces of two photonic elements or by placing them at a very short separation. Because of the wave nature of light, the transport of light between separated objects is realised by the tunnelling of photons between the two objects carrying the light. This tunnelling of light is described with the corresponding Maxwell's equations for an electromagnetic field.

There are two fundamental physical requirements that have to be fulfilled simultaneously for the transfer of electromagnetic energy between two photonic elements, for example, between a waveguide and a microcavity: (i) the electromagnetic eigenwaves in both objects must overlap in some part of the space between the two objects; (ii) the two fields must oscillate at the same frequency

and they have to be matched in their phases. The energy between the two objects is then exchanged because of the coupling of the two fields, or, more precisely, the evanescent tails of the fields oscillating inside the objects and decaying exponentially in their vicinity. Because of their technical importance, the energy transport and coupling of electromagnetic fields have been studied intensively for photonic elements based on the solid state. Here, we shall address the problem of the transfer of light between a planar optical waveguide and a spherical optical microresonator made of liquid crystals that is placed in close proximity to the waveguide.

The geometry of the problem is illustrated in Figure 27. A thin waveguide of refractive index n_s and thickness h is deposited onto a substrate of refractive index n_{sb} . A spherical microresonator of radius R_0 and refractive index n_c is in close vicinity to the waveguide, separated by a gap d , as illustrated in Figure 27. The waveguide and the microsphere are surrounded by an isotropic medium of refractive index n_{cl} .

The waveguide supports traveling TE and TM electromagnetic waves, which are the solutions of Maxwell's equations in a planar geometry. Similarly, a spherical microresonator supports its own eigenmodes, which are the corresponding solutions of Maxwell's equations in a spherically confined geometry. Because both electromagnetic fields are confined, there is an evanescent decay of the fields in the vicinity of the surface of the waveguide and the microresonator. When these two objects are close enough, the evanescent fields of both objects start

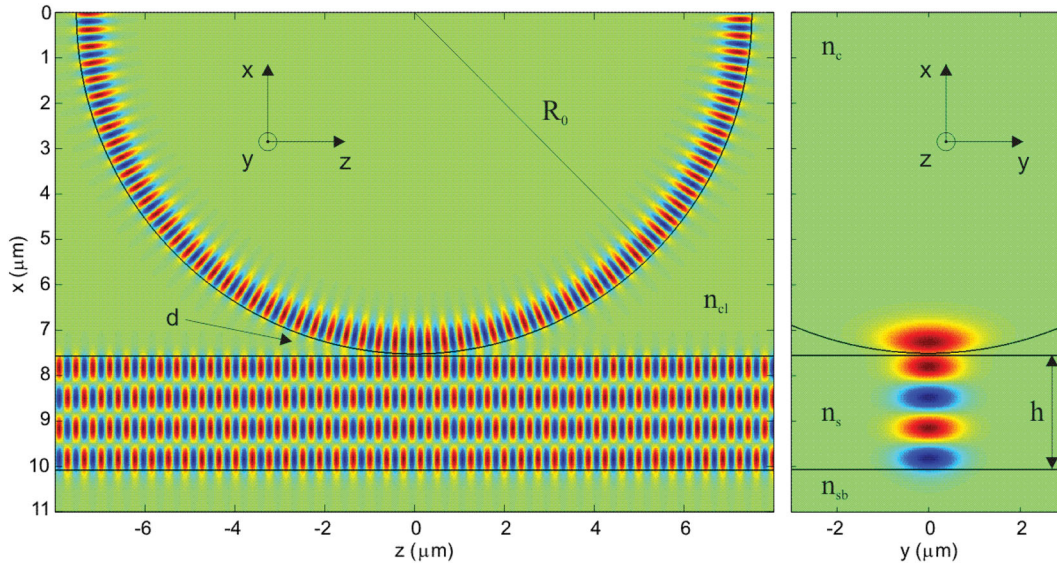


Figure 27. Schematics of the spherical microresonator, separated by a gap d from the planar waveguide below. The real part of the electric field of light in the cavity and in the slab waveguide is shown. The mode in the 15- μm -diameter cavity corresponds to the mode numbers $n = 1$ and $l = m = 125$, whereas the mode in the 2.5- μm -thick waveguide corresponds to the mode number $q = 3$. (a) Cross-section in the plane parallel to the propagation of light that goes through the point of closest separation. (b) Cross-section in the plane perpendicular to the propagation of light. Reprinted with permission of Optical Society of America, Ref. [108].

to overlap, which results in a coupling between the eigenmodes of each system. Strictly speaking, we would have to find new eigensolutions of a coupled system of two objects. However, we can construct approximate solutions of the electromagnetic waves of the coupled system in a first-order approximation. The approximate solution will be a linear combination of the two isolated eigensolutions, using a standard perturbative approach. This coupled-mode approach is used in many areas of physics and the corresponding mathematical formalism is well known. The most important parameter here is the overlapping integral, which measures the extent and the strength of the coupling of two isolated systems.

Within the coupled-mode approach, we start with a set of eigensolutions of Maxwell's equations in the planar waveguide [106] and in the spherical isotropic resonator,[107] which are well known. The calculated electromagnetic fields (see Figure 27) emanate from the surface of the waveguide and the microsphere, and decay exponentially into the surrounding medium.[108] The penetration lengths depend on the material's parameters and are typically in the range of 100 nm. These evanescent, exponentially decaying fields are therefore the only source of coupling between the light fields in the waveguide and the microcavity. Their spatial and temporal overlapping determines the degree of coupling and consequently the amount of energy that can be transferred between the waveguide and the microresonator.

The overlap of the two electric fields is characterised by calculating the integral in the (x,y) plane, which is

perpendicular to the direction of propagation, z :

$$\eta_{sc}(z) = \frac{\omega \epsilon_0}{4} N_s N_c \int \int_{\text{cavity}} (n_c^2 - n_{cl}^2) \vec{E}_c \cdot \vec{E}_s dx dy. \quad (1)$$

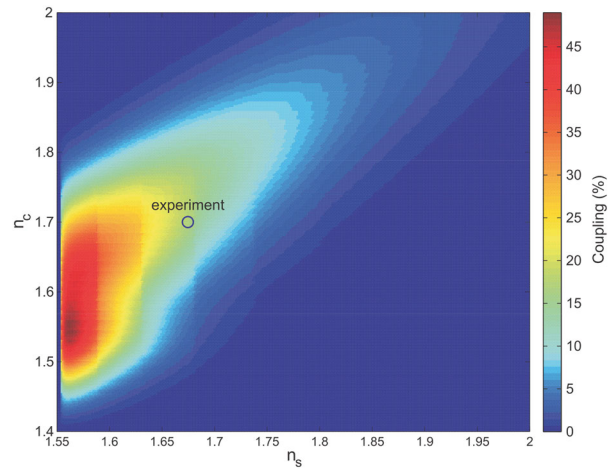


Figure 28. Calculated coupling efficiency for resonant-light transport between the slab waveguide of refractive index n_s and an isotropic spherical cavity of refractive index n_c at a fixed surface-to-surface separation of 50 nm. The highest coupling of nearly 50% is achieved for small refractive indices of the slab ($n_s = 156$), where a single-mode propagation is achieved. The circle shows the values of the indices of both materials used in the experiment, as explained in the continuation. In the experiment, we expect a coupling efficiency of 20%. Reprinted with permission of Optical Society of America, Ref. [108].

Here, the subscripts “s” and “c” denote the slab and the cavity, respectively, N_c and N_s are the normalisation constants, and \vec{E}_c and \vec{E}_s are the electric fields of the eigenmodes in the waveguide and the microsphere, respectively. The degree of coupling between the waveguide and the microsphere is determined by the coupling coefficient κ , which is calculated by integrating $\eta_{sc}(z)$ along the direction of light propagation (z), while taking into account the phase mismatch:

$$\kappa = \int_{-\infty}^{+\infty} \sqrt{\eta_{sc}(z) \cdot \eta_{cs}(z)} \cdot \exp[i(\beta_s - \beta_{c,\text{eff}}(z))] dz. \quad (2)$$

While moving from the point of closest separation, the overlap integral $\eta_{sc}(z)$ rapidly decreases because the evanescent fields decay exponentially the further they are from the surface. At the same time, the mismatch of the phases of the two light fields results in rapid spatial oscillations, which also reduce the coupling efficiency. The two propagation constants β_s and β_c should be as close

as possible in order to minimise the phase mismatch of the two light fields and to maximise the coupling. This can be done by selecting an appropriate refractive index and thickness for the waveguide.

To find the optimum parameters for the resonant light transfer, the coupling efficiency was calculated for different refractive indices of the waveguide and the cavity, and is shown in Figure 28. This analysis is the first step in the preparation of the experiments on the resonant transport of light. Fine tuning of the refractive indices of both the waveguide and the microresonator are crucial for the efficient transport of light between them.

The experiments on the resonant transport of light were performed using the set-up shown in Figure 29. A hybrid polymer with a high refractive index $n_s = 1.675$ was spin coated onto a microscope glass slide. The obtained thickness was $2.5 \mu\text{m}$. A prism-film coupler [109,110] was positioned on top of the polymer waveguide to transfer a spectral band of 60 nm from a super-continuum (white) laser. It was estimated that 6 modes

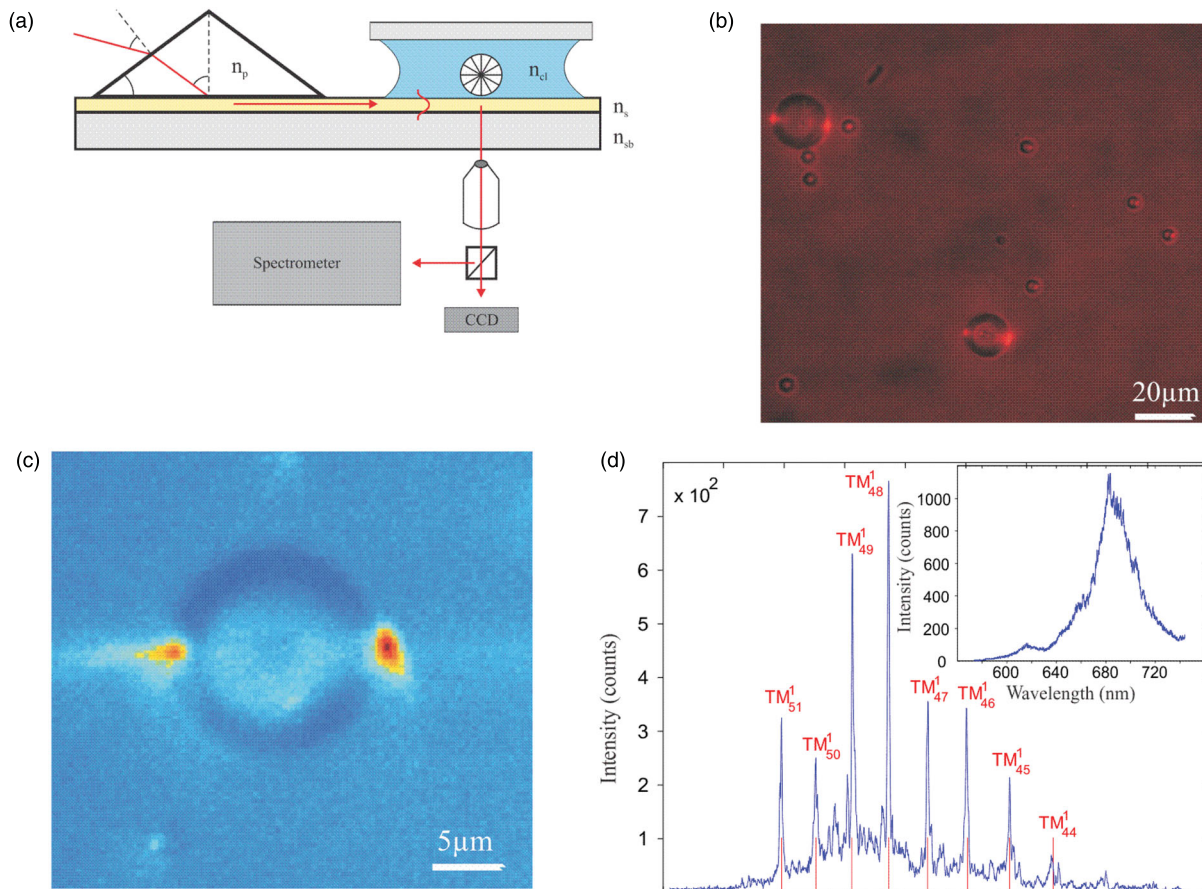


Figure 29. (a) Schematic diagram of the experimental set-up. The light is coupled to the film by a high-refractive-index prism. This light is resonantly transferred to the liquid-crystal microdroplet floating in the water. The light from this droplet is captured by the microscope objective and spectrally analysed. (b) Image of 5CB microdroplets floating in water-SDS solution. We can clearly see reddish spots at the equator of each droplet, indicating the WGMs in the droplet. (c) Spectral image showing the intensity of the light emitted from the microdroplet. Note the two bright spots due to the emission from the WGMs. (d) Spectrum of light from a 6- μm -diameter 5CB droplet, which demonstrates the WGM resonances. Reprinted with permission of Optical Society of America, Ref. [108].

could be guided in this polymer film on the glass. A small glass cell was constructed near the prism coupler, which was filled with a water dispersion of liquid-crystal microdroplets, as shown in Figure 29.

Because of gravity, the larger droplets of 5CB gradually precipitate to the bottom of the measuring cell, which is the surface of the waveguiding-polymer film. In this situation, we can clearly observe bright spots on the droplets, which confirm that light has been transferred from the polymer waveguide into the liquid-crystal droplets. The transferred light is circulated inside the droplets in the form of WGMs. Because these are leaky modes, some light is emitted from the droplets and can be observed as a bright spot shining towards the microscope objective. Smaller droplets show only one bright spot on the far side of the droplet, which indicates an immediate leaking of the light out of the droplet after it is resonantly transferred to the droplet.

The analysis of the spectrum of emitted light from these bright spots is shown in Figure 29(d) and clearly indicates WGM resonances. Although this experiment is far from being optimised in terms of refractive indices and maximum coupling, it demonstrates a proof-of-principle that light can be resonantly transferred between soft-matter objects of different shapes in close proximity.

11. Fast and ultra-fast all-optical response of a nematic liquid crystal

Liquid crystals are superior optical materials for large-area displays, but it is generally considered that their collective and slow millisecond response makes them useless for ultra-fast optical applications. However, it was overlooked in the past that liquid crystals could in fact respond optically very quickly, even on a sub-picosecond timescale, although it is well-known that in ordinary liquids, it is possible to induce the ultra-fast Kerr effect using the strong electric field of the optical impulse.

When considering the application of liquid-crystal microphotonic devices, which have already been explained in this paper, in fast (gigahertz) and ultra-fast (terahertz) integrated optical circuits, there are actually (at least) two options:

- (i) Modulation of the refractive index of a material that forms the gap between two evanescently coupled liquid-crystal micro-elements (such as a fibre and a sphere) by an intense, ultra-fast laser impulse. This modulation will induce a change in the coupling of the two elements and therefore changed the conditions for the resonant transfer of light from one element to the other. This concept is energetically extensive, since strong pulses (millijoule of energy

per pulse) are needed to change the refractive index by a significant amount, i.e., of the order of 10^{-4} .

- (ii) Instead of using strong optical pulses to change the refractive index, and consequently the optical resonance conditions, or to re-direct the light, we could use fluorescence to generate short optical pulses, whose flow could be controlled by the STimulated-Emission Depletion (STED) effect. This effect was used by S. W. Hell and J. Wichmann in 1994 [111] as a method for bypassing the refraction limit of an optical microscope. It will be shown in the continuation that STED could be used for the nanosecond control and optical pulse shaping in a fluorescently doped liquid crystal.

It was demonstrated in the 1990s that nano- and picosecond-induced molecular orientation in nematic liquid crystals and dye-doped nematic liquid crystals could result in the very fast, all-optical response of a nematic liquid crystal as a result of the optical Kerr effect. [112–121] However, no quantitative measurements of the induced refractive index were reported, which made it difficult to consider the optical Kerr effect as a candidate for the ultra-fast, all-optical control of light in microphotonic devices based on liquid crystals. Recently, Borshch et al. [122] demonstrated the tens-of-nanoseconds response of the refractive index of a nematic liquid crystal by applying an intense electric field to a thin layer of a nematic liquid crystal. The applied electric fields were of the order of $100 \text{ V}/\mu\text{m}$, and the field was applied using standard transparent indium-tin-oxide electrodes. Driving the fast optical response of a liquid crystal by applying the electric charge in a capacitance-resistor geometry has inherent limitations because of the time constant of such an electric circuit. It causes electrical latency and delays, which are well known in fast microprocessor devices and circuitry.

The origin of this nanosecond response is in the enhanced degree of orientational order of the liquid-crystal molecules. The molecules are forced to align along the strong electric field that temporarily changes the molecular orientational distribution. In terms of phase transitions and order parameters in the nematic liquid crystal, such an intense electric field couples quadratically to the magnitude of the order parameter S and induces a very fast transient refractive index. Alternatively, this can be considered as a coupling of the external electric field to the order parameter modes, known as the “hard modes” of the tensorial order parameter. The relaxation frequencies of these modes are typically in the megahertz to gigahertz spectral region, which roughly corresponds to the timescale of the transient phenomena observed by Borshch et al.

On the other hand, in ordinary liquids the electric field of a strong light pulse is known to modify the refractive index of the liquid via the optical nonlinear Kerr effect on a timescale of 100 fs to a picosecond. In this nonlinear process, the electric field of light is directly affecting the molecular electron-density distribution, while other molecular degrees of freedom remain unaffected. The ultra-fast nonlinear response is thus orders of magnitude faster than other optical phenomena in liquids. Because of the ultra-fast response of the molecular electron density, the liquid can be considered as frozen in time, since other degrees of freedom are not important for such short times. Another advantage of the optical Kerr effect is that the electric field is applied in a contactless manner via the electromagnetic wave and has no limitations in terms of pulse duration.

It was recently reported that it is possible to induce an ultra-fast change of the refractive index of a typical nematic liquid crystal 5CB of the order of 10^{-4} on a timescale of 500 fs and at a fluence of 4 mJ/cm^2 , which corresponds to an electric field of $660 \text{ V}/\mu\text{m}$. [123] The experiment was performed on a $23\text{-}\mu\text{m}$ -thick planar cell of 5CB between two quartz glass slides. The laser-induced birefringent dynamic was studied using a time-resolved stroboscopic optical pump-probe technique with an

amplified Ti:sapphire laser, as shown in Figure 30. The laser beam was split with a 85%–15% beam splitter to set up a non-collinear pump-probe scheme and the probe beam was doubled in frequency with a nonlinear barium-boron-oxide crystal. Both beams were linearly polarised, delayed with respect to each other and superimposed on the sample.

Well within the first picosecond of the light pulse, we can clearly observe ultra-fast transience both in the normalised relative transmission of the sample (Figure 30(b)) and in the rotation of the probe beam polarisation (Figure 30(c)). The change in the transmission of the sample is the result of the refractive-index change of the sample during the application of the intense laser pulse. This nonlinear-optical-Kerr-effect-induced change of the refractive index modifies the reflectivity at the glass-cell/liquid-crystal interface, and therefore also the transmission of the sample. The optical Kerr effect response is a maximum when the pump beam is oriented along the director, and decreases strongly when the polarisation of the beam is turned perpendicularly to the director. This anisotropy of the nonlinear optical Kerr effect disappears in the isotropic phase. The experiment suggests that cyano-biphenyl liquid crystals (such as the n-CB family) are anisotropically Kerr-active in

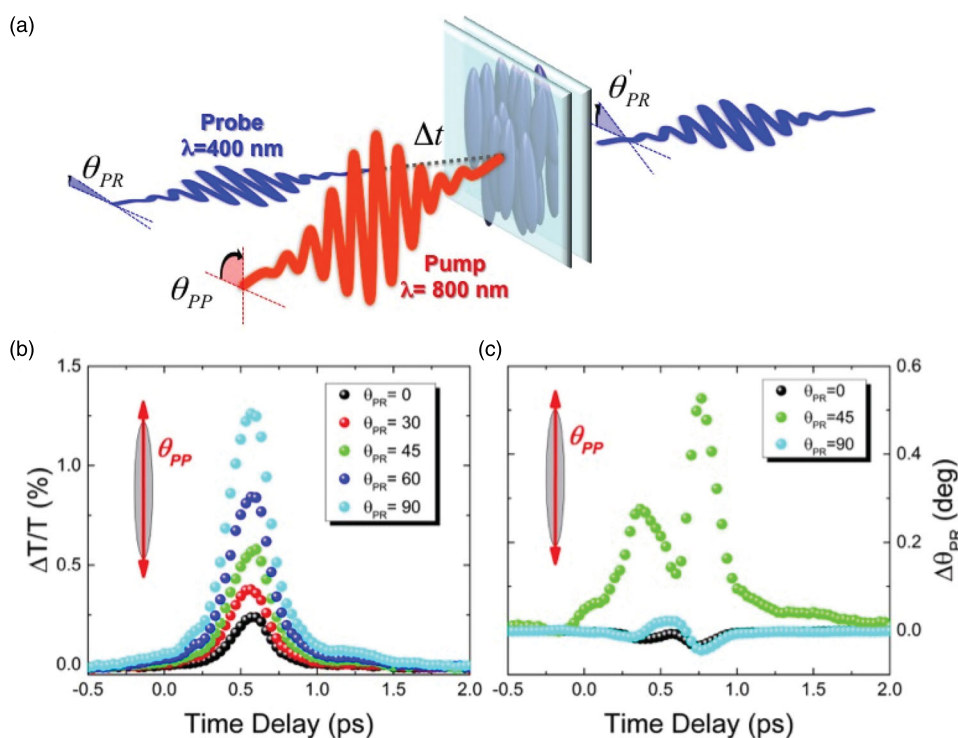


Figure 30. Ultra-fast response of a nematic liquid-crystal 5CB due to a 100-fs excitation pulse in a pump-probe experiment. (a) Scheme of the pump-probe experiment, where x is the pump linear polarisation axis and y is the probe linear polarisation axis. (b) Time dependence of the normalised relative transmission of the sample with the pump (excitation) polarisation along the director. The fluence of the pump beam is 4 mJ/cm^2 , which corresponds to an electric field of $660 \text{ V}/\mu\text{m}$. (c) Time dependence of the rotation of the polarisation of the probe beam for pump polarisation along the director. Reprinted with permission of Optical Society of America, Ref. [123].

their ordered phase and that the dominant Kerr contribution is obtained with the electric field of light set along the molecular axis. The Kerr-induced birefringence was estimated from the measurements of reflectivity and polarisation rotation (Figure 30(c)) to be 10^{-4} in a time of 500 fs. In contrast to the reflectivity (Figure 30(b)), the rotation of polarisation shows wing-like features, which depend on the polarisations of the pump and probe beams. The analysis shows an ultra-fast transience, which is present for all the pump polarisations and corresponds to 2.7 THz. Interestingly, the 5CB nematic liquid crystal shows its most characteristic terahertz signature exactly in this range.[124,125] This can be explained in terms of optically induced vibrational modes, i.e., intramolecular vibrations, excited through a non-resonant channel, i.e., by stimulated Raman scattering. Since the frequency bandwidth of the pulse is of the order of 3 THz, it contains both frequencies required to excite the low-frequency singular vibration modes of 5CB, collectively oscillating along the pump polarisation. When the pump polarisation is along the director, these single molecule vibrations are coherently excited and result in an enhanced optical Kerr response, oscillating at 2.7 THz.

Although the nonlinear optical response of a nematic liquid crystal to a strong optical pulse is very fast and therefore promising for photonic applications, the electric fields that are involved in these experiments are extremely high, of the order of $600 \text{ V}/\mu\text{m}$. This raises the question of whether there is another way of generating and controlling sub-nanosecond optical pulses in nematic liquid crystals using an all-optical and low-power scheme.

It is well known from fluorescence spectroscopy that it is possible to create extremely short optical pulses by the optical excitation of fluorescent molecules. These processes are very well understood and the energy scheme of fluorescent excitation and emission is shown in Figure 31.

In 1994, Hell and Wichmann proposed a new concept for the optical imaging of fluorescent samples, which allows the classic diffraction limits to be bypassed. The idea is based on using two laser beams of different colours. Both beams are pulsed beams with a sequence of very short and time-correlated light pulses. The first pulse beam is used as the fluorescence excitation beam and has a Gaussian cross-section. After pulsing through the microscope objective, it is focused on a diffraction-limited spot with a typical diameter of 250 nm. A fluorescently labelled sample is then placed in the focus of this fluorescence excitation beam. Each light pulse of the beam excites the electrons of the illuminated molecules into the upper excited level. However, before the electrons spontaneously relax into the ground state and emit fluorescent photons, another light pulse illuminates the excited area. This second light pulse has two important characteristics:

- (i) The cross-section of the second light pulse is doughnut-like; it has a bright ring and dark centre. It is generated when a Gaussian beam passes through a specially designed phase plate, which transforms the Gaussian beam into a so-called Laguerre beam. Because of the dark centre, the central region of the illuminated spot remains unaffected.

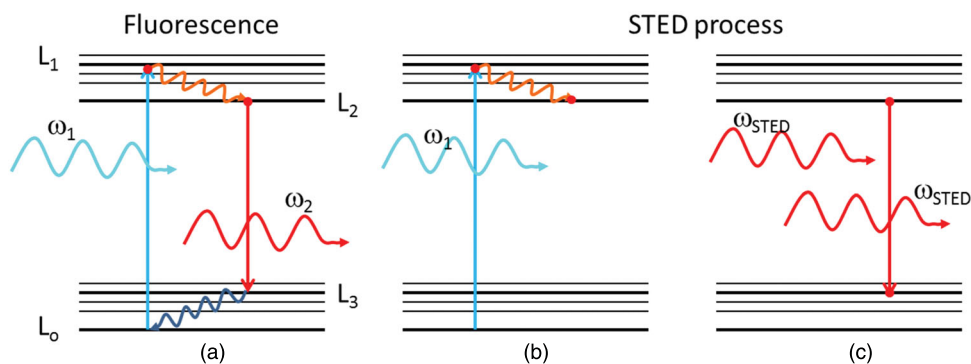


Figure 31. Schematic drawing of the electron energy levels and the electronic fluorescence transitions in a typical fluorescent molecule. (a) An electron from the molecular ground state L_0 is excited via the absorption of a blue photon ω_1 from the fluorescence excitation source. Once in the upper energy level L_1 , the electron relaxes via molecular vibrational levels to the lowest energy of the excitation band L_2 . From this state, the electron is relaxed back to the ground electronic state via the emission of a red-shifted photon ω_2 . This process is known as a fluorescence. (b) In an STED process, the electrons are first excited to the upper molecular levels via blue photon absorption. (c) When in the excited state, before the spontaneous fluorescence takes place, a resonant STED beam is sent to the fluorophores, which induces the stimulated transition of electrons from the excited to the ground state. Each STED photon creates an identical photon with stimulated emission.

- (ii) The wavelength of the second light pulse (typical duration 100 ps) is selected so that it causes stimulated emission from the electrons in the excited molecular levels. Remember that this second pulse hits the excited molecules before they had enough time to spontaneously emit the fluorescent photons. In the stimulated emission, each photon creates an exact copy of itself, which means that the second pulse takes the light away along the direction of its propagation. In the microscope setup, we observe the fluorescent reflectivity of the sample, which means that this stimulated emission will take the light away from the direction of observation. However, this will only happen for the illuminated ring of the Laguerre beam. The centre, which is dark, will of course emit the fluorescent light, since it was not affected by the STED pulse.

The dimension of the dark centre of the Laguerre beam is well below 100 nm, which means that the fluorescence will be emitted from very small spots, much smaller than the classic diffraction limit. The typical size

is 20–30 nm. By scanning the STED system across the sample, we can acquire the fluorescent image of the sample with a resolution well beyond the classic diffraction limit. We can see from the description of the STED microscopy that it involves the control of light by light on a fluorescent source. The STED impulse plays the role of the gate-controlling pulse, which can switch the fluorescent light on and off.

The idea of controlling the fluorescence of the sample via the STED mechanism was recently used for nanosecond control and optical pulse shaping by STED in a nematic liquid crystal.[126] The fluorescent sample was an 8CB liquid crystal that is in the smectic-A phase at room temperature. A small amount of fluorescent Nile-red dye was added to the 8CB. This molecule is known to align its radiative dipole moment along the long axis of the 8CB molecules. In a planar cell, the liquid-crystal molecules as well as the dye molecules are aligned along the rubbing direction. We expect a strongly polarised STED effect in such a sample.

The STED setup is presented in Figure 32. The light source is a pulsed supercontinuum laser, which emits

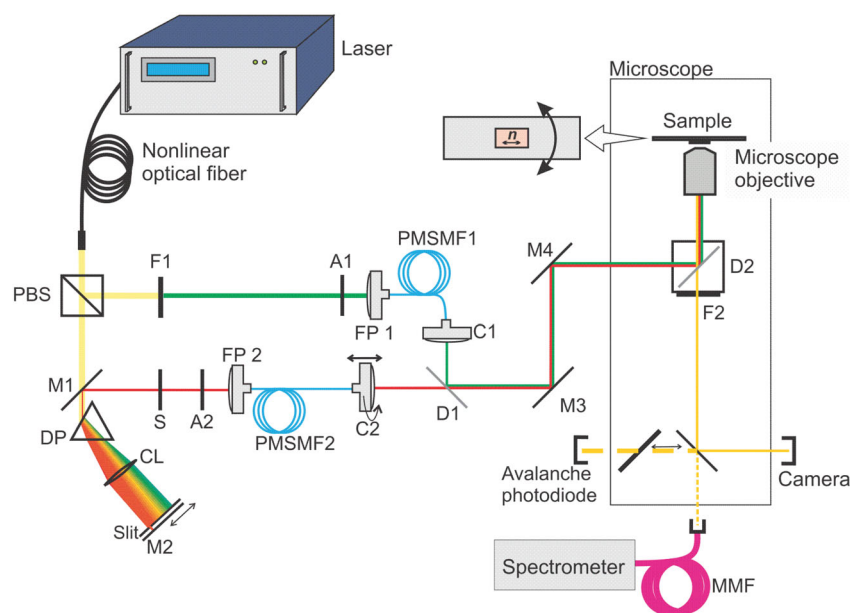


Figure 32. Setup for the STED experiment. White light from the laser is split into two beams of perpendicular polarisations by a polarising beam-splitter. For the excitation beam (green), we chose the wavelength band with a bandpass filter (F1). The beam passes through a continuous neutral density attenuator (A1) and is coupled into a polarisation-maintaining single-mode optical fibre (PMSMF1). The light is collimated at the fibre output. The STED beam wavelength (red) is chosen by a dispersing-prism-based wavelength selector by simply changing the position of the slit. This beam also passes through a continuous attenuator (A2) and is coupled into the polarisation-maintaining single-mode fibre (PMSMF2) to be cleaned of higher optical modes. Collimator C2 is mounted so that it can be translated along the optical axis and rotated around it. This enables a change of the optical path and the rotation of the STED beam polarisation. After collimation at the fibre outputs, both beams are joined by a dichroic mirror (D1) that reflects wavelengths shorter than 638 nm. The beams are carefully aligned and sent into the microscope through its backport. They are both reflected to the sample on a dual-edge dichroic mirror (D2) and focused through a 60 \times water-immersion objective. The fluorescence (yellow) is transmitted through the dual-edge dichroic mirror (D2) and bandpass filter (F2) and sent to one of the detectors. M1, M2, M3, M4: mirrors, DP: dispersive prism, CL: cylindrical lens, S: shutter, FP1, FP2: fibre ports, MMF: multi-mode fibre. Reprinted with permission of Optical Society of America, Ref. [126].

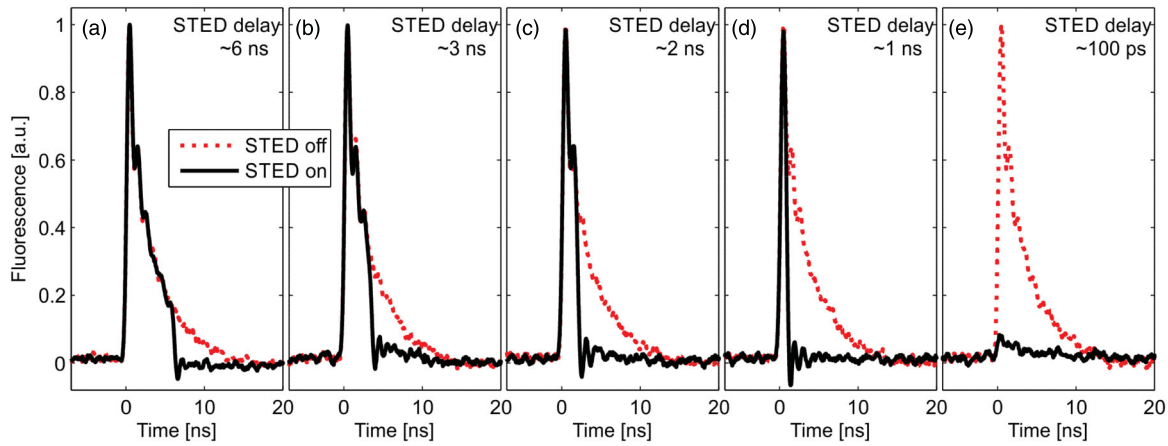


Figure 33. Controlled shortening of the emitted fluorescence by applying a time-delayed STED pulse. (a) The STED pulse was delayed for 6 ns. Note the sudden decrease of the fluorescence to zero after a 150-ps STED pulse was applied. The delay time of the STED pulse was gradually shortened in (b)–(e), which resulted in shortening of the emitted fluorescent light. The delay time was roughly estimated from the optical path measurement with an uncertainty of 50 ps. The red dotted line shows the spontaneous fluorescence when no STED pulse is applied. Reprinted with permission of Optical Society of America, Ref. [126].

unpolarised white laser light within a continuous spectrum ranging from blue to infrared. The pulse width of the pulsed laser is 150 ps and the repetition rate is 1 MHz. The beam is split into two beams of perpendicular linear polarisations, one of which serves as a fluorescence-excitation beam and the other as an STED beam. The wavelengths of the excitation and the STED beams are selected and delayed with respect to each other with a tuneable delay line. Afterwards, these two beams are recombined, centred, and sent to the fluorescent 8CB sample through the microscope objective. The illuminated spot is then either observed through a camera or analysed with a fast digital oscilloscope.

Details of the STED imaging characteristic, such as the polarisation dependence in the smectic-A, nematic and isotropic phase, can be found in [126]. Here, we will concentrate on the time characteristics of STED, which are presented in Figure 33. In this set of oscilloscope images, the STED pulse is delayed by a variable time, starting from 6 ns in Figure 33(a) and ending at 100 ps in Figure 33(e). We can clearly see the effect of the incoming STED impulse, which instantaneously darkens the fluorescence emission. By shortening the delay time, the remaining fluorescent impulse becomes shorter and shorter, until at a 100-ps delay we lose the fluorescent signal completely. This is clear evidence that it is possible to generate, in a controlled way, light impulses with a duration of at least 1 ns. In fact, this experiment is limited by the digital signal sampling, which is 4 GHz and corresponds to 250 ps. Most probably, light pulses shorter than 1 ns could be generated as well.

The STED shaping of fluorescence pulses is not limited to a single fluorescent impulse. It was demonstrated that

by splitting the fluorescent impulses into two beams with time-delayed pulses, two consequent fluorescent pulses could be controlled as well. This clearly demonstrates that arbitrary sequences of fluorescent pulses with an arbitrary delay and pulse width can be created by realising the STED control in an appropriately designed optical scheme.

12. Conclusions

The aim of this review paper was not only to present a collection of individual papers related to the microphotonics of liquid crystals, but also to give a coherent view of what integrated liquid crystal microphotonics might become in the future. The author regrets that he was unable to cover other very important aspects of photonic applications of liquid crystals, simply because of the limited length of this review paper. Many interesting photonic applications are based on macroscopic liquid-crystalline cells, where surface patterning, photoalignment and control of light by light were used [127].

These ideas were developed over the past 10 years, starting with attempts, later successful, to assemble photonic crystals from colloidal particles in nematic liquid crystals. Looking back, we can say that there was no clear roadmap, nor any very-well-developed idea of what liquid-crystal microphotonics might be. Instead, the research was driven by our curiosity about colloidal assembly in nematic liquid crystals at an early stage. Later, around 2009, the idea of using liquid crystals themselves to form spherical and cylinder-like structures was developed in detail. This resulted in the exciting observation of tuneable WGMs in nematic droplets, lasing

in nematic droplets, lasing and waveguiding in smectic microtubes and omni-directional 3D lasing from chiral nematic microdroplets.

On the other hand, the work on colloidal assembly not only resulted in the formation of nematic colloidal crystals in 2D and 3D, but also led to the discovery of the entanglement of colloidal particles by defect loops. This observation opened a completely novel direction for exploring the topological properties of nematic liquid crystals with inclusions. The strange behaviour of liquid crystals, such as the knotting and linking of colloidal particles with a single or a multitude of defect loops, is not only interesting per se, it could also be used as a mechanism for the permanent and complex binding of colloidal particles in nematic liquid crystals by defect loops. In this way, we could “reinvent” the use of ropes, which actually re-appear throughout the history of mankind in different forms. However, these are “topological” ropes, which could in future be used to bind together microphotonic elements in liquid crystals.

Of particular interest for the future of integrated microphotronics is the nature of the photonic generation, transport, and redirection of light. Unlike electrons, which can be accelerated and redirected by the force of an electric field, there is no such mechanism for photons; they cannot be accelerated or stopped by external fields and they do not interact with each other directly. This means that we need matter and the interactions of photons with matter to control the flow of photons. It seems that fluorescence is a very powerful phenomenon of this sort; it is a fast phenomenon, it uses low power and it could be designed both in terms of chemistry and material properties. In the future, fluorescence control in liquid-crystal-integrated microphotronics will most likely be used to realise fast, and presumably ultra-fast, circuitry based on self-organised liquid crystals and other forms of soft matter.

Acknowledgments

The author wishes to acknowledge the contribution to this review paper of many colleagues over many years of research: Matjaž Humar, Miha Škarabot, Andriy Nych, Ulyana Ognysta, Maruša Vitek, V.S. Rao Jampani, Slobodan Žumer, Miha Ravnik, Laura Cattaneo and Theo Rasing.

Disclosure statement

No potential conflict of interest was reported by the author.

Funding

This work was supported by the Slovenian Research Agency (ARRS) through research contracts P1-0099 and J1-6723.

References

- [1] Yablonovitch E, Gmitter, TJ. Photonic band structure: the face-centered-cubic case. *Phys Rev Lett.* **1989**;63: 1950–1953.
- [2] Yablonovitch E. Inhibited spontaneous emission in solid-state physics and electronics. *Phys Rev Lett.* **1987**;58:2059–2062.
- [3] John S. Strong localization of photons in certain disordered dielectric superlattices. *Phys Rev Lett.* **1987**;58: 2486–2489.
- [4] de Gennes PG. *The physics of liquid crystals.* Oxford: Oxford University Press; **1974**.
- [5] Muševič I, Blinc R, Žekš B. *The physics of ferroelectric and antiferroelectric liquid crystals.* Singapore: World Scientific Publishing; **2000**.
- [6] van Blaaderen A, Ruel R, Wiltzius P. Template-directed colloidal crystallization. *Nature.* **1997**;385:321–324.
- [7] Aoki K, Miyazaki HT, Hirayama H, et al. Microassembly of semiconductor three-dimensional photonic crystals. *Nature Mater.* **2003**;2:117–121.
- [8] Chiou PY, Ohta, AT, Wu MC. Massively parallel manipulation of single cells and microparticles using optical images. *Nature.* **2005**;436:370–372.
- [9] Mirkin CA, Letsinger RL, Mucic RC, Storhoff JJ. A DNA-based method for rationally assembling nanoparticles into macroscopic materials. *Nature.* **1996**;382:607–609.
- [10] Maruo S, Nakamura O, Kawata S. Three-dimensional microfabrication with two-photon-absorbed photopolymerization. *Opt Lett.* **1997**;22:132–134.
- [11] Ellis B, Mayer MA, Shambat G, et al. Ultralow-threshold electrically pumped quantum-dot photonic-crystal nanocavity laser. *Nat Photonics.* **2011**;5:297–300.
- [12] Park H-G, Barrelet CJ, Wu Y, Tian B, Qian F, Lieber CM. A wavelength-selective photonic-crystal waveguide coupled to a nanowire light source. *Nat Photonics.* **2008**;2:622–626.
- [13] Liang D, Bowers JE. Recent progress in lasers on silicon. *Nat Photonics.* **2010**;4:511–517.
- [14] Muševič I. Integrated and topological liquid crystal photonics. *Liq Cryst.* **2014**;41:418–429.
- [15] Muševič I. Nematic colloids, topology and photonics. *Phil Trans R Soc A.* **2013**;371:20120266.
- [16] Cladis PE, Pieranski P. Sur une nouvelle methode de decoration de la phase mesomorphe du MBBA. *C R Acad Sc Paris.* **1971**;273:275–280.
- [17] Rault J. Sur une methode nouvelle d'étude de l'orientation moleculaire a la surface d'un cholesterique. *C R Acad Sc Paris.* **1971**;272:1275–1281.
- [18] Poulin P, Stark H, Lubensk TC, Weitz DA. Novel colloidal interactions in anisotropic fluids. *Science.* **1997**;275:1770–1773.
- [19] Hotta Jun-ichi, Sasaki K, Masuhara H. Manipulation of liquid crystal textures with a focused near infrared laser beam. *Appl Phys Lett.* **1997**;71:2085–2087.
- [20] Juodkasis S, Iwashita M, Takahashi T, Matsuo S, Misawa H. Fast optical switching by a laser-manipulated microdroplet of liquid crystal. *Appl Phys Lett.* **1999**;74: 3627–3629.
- [21] Gleeson HF, Wood TA, Dickinson M. Laser manipulation in liquid crystals: an approach to microfluidics and micromachines. *Phil Trans R Soc A.* **2006**;364: 2789–2805.

- [22] Iwashita Y, Tanaka H. Optical manipulation of defects in a lyotropic lamellar phase. *Phys Rev Lett.* **2003**;90:045501-1-4.
- [23] Mušević I, Škarabot M, Babič D, et al. Laser trapping of small colloidal particles in a nematic liquid crystal: clouds and ghosts. *Phys Rev Lett.* **2004**;93:187801-1-4.
- [24] Smalyukh I, Kachynski AV, Kuzmin AN, Prasad PN. Laser trapping in anisotropic fluids and polarization-controlled particle dynamics. *Proc Nat Acad Sc.* **2006**;103:18048–18053.
- [25] Mušević I, Škarabot M, Tkalec U, Ravnik M, Žumer S. Two dimensional nematic colloidal crystals self-assembled by topological defects. *Science.* **2006**;313:954–958.
- [26] Škarabot M, Ravnik M, Žumer S, et al. Interactions of quadrupolar nematic colloids. *Phys Rev E.* **2007**;76:051406-1-6.
- [27] Škarabot M, Ravnik M, Žumer S, et al. Two-dimensional dipolar nematic colloidal crystals. *Phys Rev E.* **2008**;77:031705-1-8.
- [28] Ognysta U, Nych A, Nazarenko V, et al. 2D interactions and binary crystals of dipolar and quadrupolar nematic colloids. *Phys Rev Lett.* **2008**;100:217803-1-4.
- [29] Ognysta U, Nych A, Nazarenko V, Škarabot M, Mušević I. Design of 2D binary colloidal crystals in a nematic liquid crystal. *Langmuir.* **2009**;25:12092–12100.
- [30] Ryzhkova A, Mušević I. Particle size effects on nanocolloidal interactions in nematic liquid crystals. *Phys Rev E.* **2013**;87:032501-1-12.
- [31] Nych A, Ognysta U, Škarabot M, Ravnik M, Žumer S, Mušević I. Assembly and control of 3D nematic dipolar colloidal crystals *Nat. Commun.* **2013**;4:1489. doi:10.1038/ncomms2486.
- [32] Ravnik M, Škarabot M, Žumer S, et al. Entangled nematic colloidal dimers and wires. *Phys Rev Lett.* **2007**;99:247801-1-4.
- [33] Terentjev EM. Disclination loops, standing alone and around solid particles in nematic liquid crystals. *Phys Rev E.* **1995**;51:1330–1337.
- [34] Guzman O, Kim EB, Grollau S, Abbott NL, de Pablo JJ. Defect structure around two colloids in a liquid crystal. *Phys Rev Lett.* **2003**;91:235507-1-4.
- [35] Araki T, Tanaka H. Colloidal aggregation in a nematic liquid crystal: topological arrest of particles by a single-stroke disclination. *Phys Rev Lett.* **2006**;97:127801-1-4.
- [36] Žumer S. Talk given at 21st international liquid crystal conference, Keystone, Colorado, USA, July 2-7; 2006.
- [37] Tkalec U, Ravnik M, Čopar S, Žumer S, Mušević I. Reconfigurable knots and links in chiral nematic colloids. *Science.* **2011**;333:62–65.
- [38] Bouligand Y. Recherches sur les textures des états mesomorphiques. Dislocations coins et signification des cloisons de Grandjean-Cano dans les cholesteriques. *J Phys (Paris).* **1974**;35:959–981.
- [39] Jampani VSR, Škarabot M, Ravnik M, Čopar S, Žumer S, Mušević I. Colloidal entanglement in highly twisted chiral nematic colloids: twisted loops, Hopf links, and trefoil knots. *Phys Rev E.* **2011**;84:031703-1-9.
- [40] Coles H, Morris S. Liquid crystal lasers. *Nat Photonics.* **2010**;4:676–685.
- [41] Kopp VI, Fan B, Vithana HKM, Genack AZ. Low-threshold lasing at the edge of a photonic stop band in cholesteric liquid crystals. *Opt Lett.* **1998**;23:1707–1709.
- [42] Taheri B, Munoz A, Palffy-Muhoray P, Twieg R. Low threshold lasing in cholesteric liquid crystals. *Mol Cryst Liq Cryst.* **2001**;358:73–82.
- [43] Ozaki M, Kasano M, Ganzke D, Hasse W, Yoshino K. Mirrorless lasing in a dye-doped ferroelectric liquid crystal. *Adv Mater.* **2002**;14:306–309.
- [44] Ford AD, Morris SM, Pivnenko MN, Coles HJ. A comparison of photonic band edge lasing in the chiral nematic N* and smectic C* phases. *Proc SPIE.* **2004**;5289:213–220.
- [45] Schmidtke J, Stille W, Finkelmann H, Kim ST. Laser emission in a dye doped cholesteric polymer network. *Adv Mater.* **2002**;14:746–749.
- [46] Shibaev PV, Tang K, Genack AZ, Kopp V, Green MM. Lasing from a stiff chain polymeric lyotropic liquid crystal. *Macromolecules.* **2002**;35:3022–3025.
- [47] Matsui T, Ozaki R, Funamoto K, Ozaki M, Yoshino K. Flexible mirrorless laser based on a free-standing film of photopolymerized cholesteric liquid crystal. *Appl Phys Lett.* **2002**;81:3741–3743.
- [48] Shibaev PV, Madsen J, Genack AZ. Lasing and narrowing of spontaneous emission from responsive cholesteric films. *Chem Mater.* **2004**;16:1397–1399.
- [49] Ohta T, Song MH, Tsunoda Y, et al. Monodomain film formation and lasing in dye-doped polymer cholesteric liquid crystals. *Jpn J Appl Phys.* **2004**;43:6142–6144.
- [50] Finkelmann H, Kim ST, Muñoz A, Palffy-Muhoray P, Taheri B. Tunable mirrorless lasing in cholesteric liquid crystalline elastomers. *Adv Mater.* **2001**;13:1069–1072.
- [51] Shibaev PV, Kopp V, Genack A, Hanelt E. Lasing from chiral photonic band gap materials based on cholesteric glasses. *Liq Cryst.* **2003**;30:1391–1400.
- [52] Wei SKH, Chen SH, Dolgaleva K, Lukishova SG, Boyd RW. Robust organic lasers comprising glassy-cholesteric pentafluorene doped with a red-emitting oligofluorene. *Appl Phys Lett.* **2009**;94:041111.
- [53] Chanishvili A, Chilaya G, Petriashvili G, et al. Lasing in an intermediated twisted phase between cholesteric and smectic a phase. *Appl Phys Lett.* **2006**;88:101105.
- [54] Cao W, Muñoz A, Palffy-Muhoray P, Taheri B. Lasing in a three-dimensional photonic crystal of the liquid crystalline blue phase II. *Nature Mater.* **2002**;1:111–113.
- [55] Yokoyama S, Mashiko S, Kikuchi H, Uchida K, Nagamura T. Laser emission from a polymer-stabilized liquid-crystalline blue phase. *Adv Mater.* **2006**;18:48–51.
- [56] Morris SM, Ford AD, Gillespie C, Pivnenko MN, Haderl O, Coles HJ. The emission characteristics of liquid crystal lasers. *J Soc Inf Display.* **2006**;14:565–573.
- [57] Funamoto K, Ozaki M, Yoshino K. Discontinuous shift of lasing wavelength with temperature in cholesteric liquid crystal. *Jpn J Appl Phys.* **2003**;42:L1523–L1525.
- [58] Morris SM, Ford AD, Pivnenko MN, Coles HJ. Enhanced emission from liquid-crystal lasers. *J Appl Phys* **2005**;97:023103.
- [59] Huang Y, Zhou Y, Doyle C, Wu S.-T. Tuning the photonic band gap in cholesteric liquid crystals by temperature-dependent dopant solubility. *Opt Express.* **2006**;14:1236–1242.

- [60] Chanishvili A, Chilaya G, Petriashvili G, et al. Phototunable lasing in dye-doped cholesteric liquid crystals. *Appl Phys Lett*. 2003;83:5353–5355.
- [61] Furumi S, Yokoyama S, Otomo A, Mashiko S. Phototunable photonic bandgap in a chiral liquid crystal laser device. *Appl Phys Lett*. 2004;84:2491–2493.
- [62] Shibaev PV, Sanford RL, Chiappetta D, Milner V, Genack AZ. Light controllable tuning and switching of lasing in chiral liquid crystals. *Opt Express*. 2005;13:2358–2363.
- [63] Furumi S, Yokoyama S, Otomo A, Mashiko S. Electrical control of the structure and lasing in chiral photonic band-gap liquid crystals. *Appl Phys Lett*. 2003;82:16–18.
- [64] Kasano M, Ozaki M, Yoshino K, Ganzke D, Haase W. Electrically tunable waveguide laser based on ferroelectric liquid crystals. *Appl Phys Lett*. 2003;82:4026–4028.
- [65] Lin T.-H, Jau H.-C, Chen C.-H, et al. Electrically controllable laser based on cholesteric liquid crystal with negative dielectric anisotropy. *Appl Phys Lett*. 2006;88:061122.
- [66] Woltman SJ, Crawford GP. Tunable cholesteric liquid crystals lasers through in-plane switching. *Proc SPIE*. 2007;6487:64870B.
- [67] Humar M, Ravnik M, Pajk S, Mušević I. Electrically tunable liquid crystal optical microresonators. *Nat Photonics*. 2009;3:595–600.
- [68] Humar M, Mušević I. 3D microlasers from self-assembled cholesteric liquid-crystal microdroplets. *Opt Express*. 2010;18:26995–27003.
- [69] Ashkin A, Dziedzic JM. Observation of resonances in the radiation pressure on dielectric spheres. *Phys Rev Lett*. 1977;38:1351–1354.
- [70] Vahala KJ. Optical microcavities. *Nature*. 2003;424:839–846.
- [71] Kiraz A, Kurt A, Dundar MA. Simple. Largely tunable optical microcavity. *Appl Phys Lett*. 2006;89:081118–1–081118-3.
- [72] Saito M, Shimatani H, Naruhashi H. Tunable whispering gallery mode emission from a microdroplet in elastomer. *Opt Exp*. 2008;16:11915–11919.
- [73] Maune B, Lawson R, Gunn C, Scherer A, Dalton L. Electrically tunable ring resonators incorporating nematic liquid crystals as cladding layers. *Appl Phys Lett*. 2003;83:4689–4691.
- [74] Wang T.-J, Chu C.-H, Lin C.-Y. Electro-optically tunable microring resonators on lithium niobate. *Opt Lett*. 2007;32:2777–2779.
- [75] Stark H. Physics of colloidal dispersions in nematic liquid crystals. *Phys Rep*. 2001;351:387–474.
- [76] Piegdon KA, Matthias H, Meier C, Kitzerow H.-S. Tunable optical properties of photonic crystals and semiconductor microdisks using liquid crystals. *Proc SPIE*. 2008;6911:6911OJ.
- [77] Wang T.-J, Chu C.-H, Lin C.-Y. Electro-optically tunable microring resonators on lithium niobate. *Opt Lett*. 2007;32:2777–2779.
- [78] Ptasincki J, Khoo IC, Fainman Y. Enhanced optical tuning of modified-geometry resonators clad in blue phase liquid crystals. *Opt Lett*. 2014;39:5435–5438.
- [79] Ptasincki J, Kim SW, Pang L, Khoo IC, Fainman Y. Optical tuning of silicon photonic structures with nematic liquid crystal claddings. *Opt Lett*. 2013;38:2008–2010.
- [80] Ma Q, Rossmann T, Guo Z. Whispering-gallery mode silica microsensors for cryogenic to room temperature measurement. *Meas Sci Technol*. 2010;21:025310–025317.
- [81] Dong C.-H, He L, Xiao Y.-F, et al. Fabrication of high-Q polydimethylsiloxane optical microspheres for thermal sensing. *Appl Phys Lett*. 2009;94:231119.
- [82] Saito M, Shimatani H, Naruhashi H. Tunable whispering gallery mode emission from a microdroplet in elastomer. *Opt Express*. 2008;16:11915–11919.
- [83] von Klitzing W, Long R, Ilchenko VS, Hare J, Lefevre-Seguin V. Tunable whispering gallery modes for spectroscopy and CQED experiments. *New J Phys*. 2001;3:14.1–14.14.
- [84] Lin I.-H, Miller DS, Bertics PJ, Murphy CJ, de Pablo JJ, Abbott NL. Endotoxin-induced structural transformations in liquid crystalline droplets. *Science*. 2011;332:1297–1300.
- [85] Manna U, Zayas-Gonzalez YM, Carlton RJ, Caruso F, Abbott NL, Lynn DM. Liquid crystal chemical sensors that cells can wear. *Angew Chem- Int Edt*. 2013;52:14011–14015.
- [86] Carlton RJ, Hunter JT, Miller DS, et al. Chemical and biological sensing using liquid crystals. *Liq Cryst Rev*. 2013;1:29–51.
- [87] Kurik MV, Lavrentovich OD. Topological defects of cholesteric liquid crystals for volumes with spherical shapes. *Mol Cryst Liq Cryst, Lett Sect*. 1982;72:239–246.
- [88] Xu F, Crooker PP. Chiral nematic droplets with parallel surface anchoring. *Phys Rev E*. 1997;56:6853–6860.
- [89] Bezič J, Žumer S. Structures of the cholesteric liquid crystal droplets with parallel surface anchoring. *Liq Cryst*. 1992;11:593–419.
- [90] Bouligand Y, Livolant F. The organization of cholesteric spherulites. *J Phys*. 1984;45:1899–1923.
- [91] Robinson C, Ward JC, Beevers RB. Liquid crystalline structure in polypeptide solutions. Part 2. *Discuss Faraday Soc*. 1958;25:29–42.
- [92] Bajc J, Bezič J, Žumer S. Chiral nematic droplets with tangential anchoring and negative dielectric anisotropy in an electric field. *Phys Rev E*. 1995;51:2176–2189.
- [93] Seč D, Porenta T, Ravnik M, Žumer S. Geometrical frustration of chiral ordering in cholesteric droplets. *Soft Matter*. 2012;8:11982–11988.
- [94] Gardiner DJ, Morris SM, Hands PJW, et al. Paintable band-edge liquid crystal lasers. *Opt Express*. 2011;19:2432–2439.
- [95] Cipparrone G, Mazzulla A, Pane A, Hernandez RJ, Bartolino R. Chiral self-assembled solid microspheres: a novel multifunctional microphotonic device. *Adv. Mat*. 2011;23:5773–5778.
- [96] Donato MG, Hernandez J, Mazzulla A, et al. Polarization-dependent optomechanics mediated by chiral microresonators. *Nature Comm*. 2014;5:Article Number: 3656.
- [97] Tkachenko G, Brasselet E. Helicity-dependent three-dimensional optical trapping of chiral microparticles. *Nature Comm*. 2014;5:Article Number: 4491.

- [98] Hamley W, Castelletto V. Biological soft materials. *Angew Chem Int Ed*. 2007;46:4442–4455.
- [99] Reissig L, Fairhurst DJ, Leng J, Cates ME, Mount AR, Egelhaaf SU. Three-dimensional structure and growth of myelins. *Langmuir*. 2010;26:15192–15199.
- [100] Pratibha R, Madhusudana NV. Cylindrical growth of smectic a liquid crystals from the isotropic phase in some binary mixtures. *J Phys II France*. 1992;2:383–400.
- [101] Peddireddy K, Kumar P, Thutupalli S, Herminghaus S, Bahr Ch. Solubilization of thermotropic liquid crystal compounds in aqueous surfactant solutions. *Langmuir*. 2012;28:12426–12431.
- [102] Peddireddy K, Jampani VSR, Thutupalli S, Herminghaus S, Bahr Ch, Musevic I. Lasing and waveguiding in smectic a liquid crystal optical fibers. *Opt Express*. 2013;21:30233. doi:10.1364/OE.21.030233.
- [103] Brasselet E, Murazawa N, Misawa H, Juodkazis S. Optical vortices from liquid crystal droplets. *Phys Rev Lett*. 2009;103:103903-1-4.
- [104] Brasselet E. Tunable optical vortex arrays from a single nematic topological defect. *Phys Rev Lett*. 2012;108:087801-1-4.
- [105] Ackerman PJ, Qi Z, Smalyukh II. Optical generation of crystalline, quasicrystalline, and arbitrary arrays of torons in confined cholesteric liquid crystals for patterning of optical vortices in laser beams. *Phys Rev E*. 2012;86:021703-1-14.
- [106] Kawano K, Kitoh T. Introduction to optical waveguide analysis. New York: Wiley-Interscience; 2001.
- [107] Bohren CF, Huffman DR. Absorption and scattering of light by small particles. Chichester, UK: Wiley Science; 1998.
- [108] Jampani VSR, Humar M, Mušević I. Resonant transport of light from planar polymer waveguide into liquid-crystal microcavity. *Opt Express*. 2013;21:20506–20516.
- [109] Ulrich R, Torge R. Measurement of thin film parameters with a prism coupler. *Appl Opt*. 1973;12:2901–2908.
- [110] Tien PK. Light waves in thin films and integrated optics. *Appl Opt*. 1971;10:2395–2413.
- [111] Hell SW, Wichman J. Breaking the diffraction resolution limit by stimulated emission: stimulated emission-depletion fluorescence microscopy. *Opt Lett*. 1994;19:780–782.
- [112] Khoo I.-C, Michael RR, Yan P. Optically-induced molecular reorientation in nematic liquid crystals and nonlinear optical processes in the nanoseconds regime. *IEEE J Quantum Electron*. 1987;23:267–272.
- [113] Eichler HJ, Macdonald R. Flow-alignment and inertial effects in picosecond laser-induced reorientation phenomena of nematic liquid crystals. *Phys Rev Lett*. 1991;67:2666–2669.
- [114] Lucchetti L, Fedorenko D, Francescangeli O, Reznikov Y, Simoni F. Surface reorientation induced by short light pulses in doped liquid crystals. *Opt Lett*. 2003;28:1621–1623.
- [115] Deeg FW, Stankus JJ, Greenfield SR, Newell VJ, Fayer MD. Anisotropic reorientational relaxation of biphenyl: transient grating optical Kerr effect measurements. *J Chem Phys*. 1989;90:6893–6902.
- [116] Truong TV, Shen YR. Resonance-enhanced optical reorientation of molecules in liquids via intermolecular interaction. *Phys Rev Lett*. 2007;99:187802-1-4.
- [117] Deeg FW, Greenfield SR, Stankus JJ, Newell VJ, Fayer MD. Nonhydrodynamic molecular motions in a complex liquid: temperature dependent dynamics in pentylcyanobiphenyl. *J Chem Phys*. 1990;93:3503–3514.
- [118] Gottke SD, Cang H, Bagchi B, Fayer MD. Comparison of the ultrafast to slow time scale dynamics of three liquid crystals in the isotropic phase. *J. Chem. Phys*. 2002;116:6339–6347.
- [119] Cang H, Li J, Novikov VN, Fayer MD. Dynamics in supercooled liquids and in the isotropic phase of liquid crystals: a comparison. *J Chem Phys*. 2003;118:9303–9311.
- [120] Hunt NT, Jaye AA, Meech SR. Ultrafast dynamics in complex fluids observed through the ultrafast optically-heterodyne-detected optical-Kerr-effect (OHD-OKE). *Phys Chem Chem Phys*. 2007;9:2167–2180.
- [121] Le Calvez A, Montant S, Freysz E, Ducasse A, Zhuang XW, Shen YR. Ultrashort orientational dynamics of liquid crystals in the smectic-a phase. *Chem Phys Lett*. 1996;258:620–625.
- [122] Borshch V, Shiyankovskii SV, Lavrentovich OD. Nanosecond electro-optic switching of a liquid crystal. *Phys Rev Lett*. 2013;111:107802-1-4.
- [123] Cattaneo L, Savoini M, Mušević I, Akimel A, Rasing Th. Ultrafast all-optical response of a nematic liquid crystal. *Opt Express*. 2015;23:14010–14017.
- [124] Vieweg N, Jansen C, Shakfa MK, et al. Molecular properties of liquid crystals in the terahertz frequency range. *Opt Express*. 2010;18:6097–6107.
- [125] Vieweg N, Fischer BM, Reuter M, et al. Ultrabroadband terahertz spectroscopy of a liquid crystal. *Opt Express*. 2012;20:28249–28256.
- [126] Vitek M, Mušević I. Nanosecond control and optical pulse shaping by stimulated emission depletion in a liquid crystal. *Opt Letters*. 2015;23:16921–16932.
- [127] Chigrinov VG, Kozenkov VM, Kwok H-S. Photoalignment of liquid crystalline materials: physics and applications. Chichester, UK: John Wiley & Sons, Ltd.; 2008.